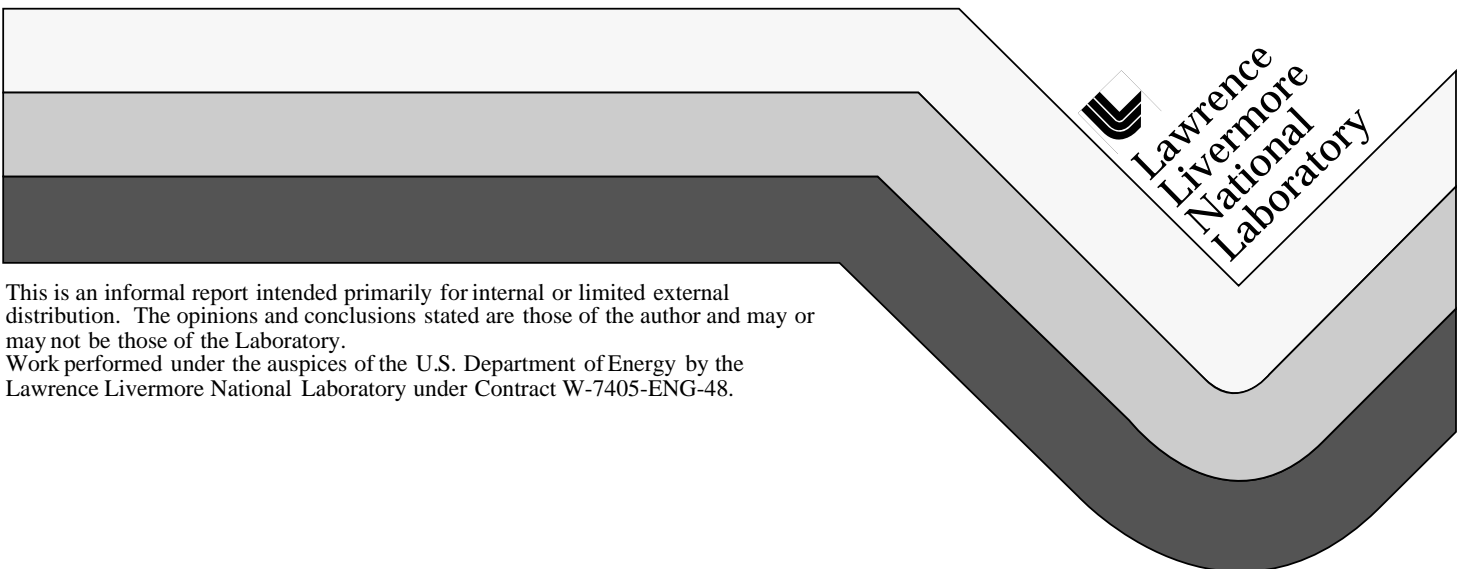


On the Role of Mass Diffusion and Fluid Dynamics in the Dissipation of Chunk Mix

Lawrence D. Cloutman

March 1999



DISCLAIMER

This document was prepared as an account of work sponsored by an agency of the United States Government. Neither the United States Government nor the University of California nor any of their employees, makes any warranty, express or implied, or assumes any legal liability or responsibility for the accuracy, completeness, or usefulness of any information, apparatus, product, or process disclosed, or represents that its use would not infringe privately owned rights. Reference herein to any specific commercial product, process, or service by trade name, trademark, manufacturer, or otherwise, does not necessarily constitute or imply its endorsement, recommendation, or favoring by the United States Government or the University of California. The views and opinions of authors expressed herein do not necessarily state or reflect those of the United States Government or the University of California, and shall not be used for advertising or product endorsement purposes.

This report has been reproduced
directly from the best available copy.

Available to DOE and DOE contractors from the
Office of Scientific and Technical Information
P.O. Box 62, Oak Ridge, TN 37831
Prices available from (423) 576-8401

Available to the public from the
National Technical Information Service
U.S. Department of Commerce
5285 Port Royal Rd.,
Springfield, VA 22161

Lawrence Livermore National Laboratory Report
UCRL-ID-133412
March 1999

ON THE ROLE OF MASS DIFFUSION AND FLUID DYNAMICS IN THE DISSIPATION OF CHUNK MIX

Lawrence D. Cloutman

Lawrence Livermore National Laboratory

Abstract

When numerically simulating multicomponent turbulent flows, subgrid-scale diffusion of chemical species requires closure. This mixing of chemical species at the molecular level dissipates concentration fluctuations, which limits possible demixing and affects other processes such as energy transport and reaction rates at the subgrid level. We discuss some of the physical processes that reduce small chunks of a heavy material in a light gas or plasma to a mixture at the atomic level. Preliminary direct numerical simulations of these processes are presented using the dissipation of small spheres of heavy gas in a light gas as an archetypal process in turbulent micromixing in multicomponent flows, including classical fluid instabilities and shock ejecta. We use a detailed approach for the diffusion process, directly solving the Stefan-Maxwell equations for the mass fluxes. We discuss the dissipation of a $24\mu\text{m}$ sphere of xenon in helium in three different flow regimes, and we present suggestions for future work intended as input to improved subgrid-scale turbulence models.

1 Introduction

Turbulent mixing plays a fundamental role in a wide variety of applications. An important application that contains all of the complexity and richness of phenomena of this process is the implosion of an inertial confinement fusion (ICF) target. A typical target is a small (on the order of 1 mm) hollow sphere consisting of one or more layers of solid material filled with a deuterium-tritium mixture (for example [1]). A set of laser beams (directly or indirectly) uniformly illuminates the sphere and ablates the outer surface. The reaction force to the ablation flow implodes the shell, sending a converging shock wave into the target. It has long been known that this system is subject to fluid dynamical instabilities [2, 3, 4, 5, 6] that produce and mix small “chunks” of shell material into the fuel. These chunks take the form of small blobs and filaments down to scales limited by molecular diffusion. This mixing of shell material and DT gas can have a deleterious effect on the thermonuclear yield and affects heat transfer, so understanding the process in all its complexity is important.

The same mixing processes occur in other situations. For example, laser imaging of the instantaneous state of a turbulent jet shows a lot of irregular, fine-scale structure as the jet entrains the ambient medium and mixes it to the jet core [7]. This is an important aspect of turbulent jet flames, which have wide industrial application. Also, the Richtmyer-Meshkov instability in a shock tube produces very small composition fluctuations in the form of blobs and filaments as the bubbles and spikes become turbulent [8]. Molecular diffusion plays an important role in the decay of the instability, in the rate at which reactions can occur between the two materials, and in the computation of opacities and other transport coefficients for large eddy simulations (LES).

This report presents some preliminary work on just one aspect of the mix problem: how chunks of shell material mix with the gas at the atomic level once the chunks get hot enough to vaporize. We shall consider both molecular diffusion and fluid dynamical processes, but under idealized conditions that make the problem tractable. We limit the present discussion to spherical chunks and relatively low-speed flows. The most significant restriction is to temperatures and pressures low enough that ionization may be ignored. Although we shall eventually need to consider more extreme conditions, the present work

illustrates some of the basic physics of the mixing process at the dissipation scale.

There are two separate cases that need to be considered. First, there may be sharp interfaces maintained between the materials, such as at the surface of a metal plate immersed in a fluid or the interface between immiscible liquids. Second, there may be no permanent physical interface, as in the case of two layers of different gases or plasmas. Even if there is a discontinuity in the initial composition, the discontinuity will immediately disappear via molecular mass diffusion. Of course, both cases may be present simultaneously in some physical systems.

In computational models of systems with sharp interfaces between pieces of solid material and between solids and liquids, the interface is often explicitly tracked using a method such as VOF [9] if the pieces of both materials are being resolved by the numerical method. If the pieces of one material are not resolvable, such as happens with the fuel spray droplets in a diesel engine, a subgrid-scale (SGS) model must be developed [10]. In many models, no exchange of material is allowed across the interface. However, in some cases, such as the diesel spray, mass exchange is crucial [11, 12], and a variety of phase-change processes may have to be considered, including freezing, melting, sublimation, evaporation, boiling, and radiatively-driven ablation.

In other systems, the two materials are gases or plasmas, and there is no physical interface. Molecular mass diffusion and thermal conduction rapidly eliminate any discontinuities in composition and temperature. This is the case we shall concentrate on in this report. Even if one material was originally solid or liquid, as soon as the condensed phase gets hot enough, it turns to vapor or plasma and loses its cohesiveness. Liquids that get above the critical temperature and pressure bypass the evaporative processes, eliminating any surface tension or material strength, and the two materials immediately begin mixing at the atomic level.

We shall consider the processes that can affect the rate of mixing and the time scales at which mixing occurs. We use the COYOTE computational fluid dynamics program [13] to study the dissipation of small chunks of heavy gas immersed in light gas. Molecular diffusion without fluid motions provides an upper bound on the dissipation time scale for chunks of various sizes, shapes, and physical conditions. Then we shall consider what happens in the

presence of streaming flow and a shock wave. These flows will accelerate the mixing process by distorting the chunk into a flattened, thinner shape and by sweeping away material until the remnant begins moving along with the ambient flow. Thereafter dissipation occurs only through diffusion.

Section 2 discusses some relevant dimensionless parameters and give some order of magnitude estimates of time scales for these processes. Section 3 summarizes the governing equations for a continuum model of chunk dissipation. Sections 4-6 present numerical examples from COYOTE. Section 7 discusses the implications of these results.

2 Order of Magnitude Estimates

Before we get into detailed simulations of the breakdown of a chunk of fluid, we consider the relevant dimensionless parameters and order of magnitude estimates of some of the time scales. Since we will be considering some very small chunks (as small as $1\text{ }\mu\text{m}$), it is necessary to estimate the Knudsen number, $\text{Kn} = \lambda/L$, where λ is the molecular mean free path and L is the size of the chunk. It is necessary for Kn to be much less than unity for the usual continuum approximation to be valid. In air under standard conditions, the mean free path is approximately $0.1\text{ }\mu\text{m}$. In this case, the continuum approximation is marginal for a $1.0\text{ }\mu\text{m}$ particle.

Let us consider a spherical chunk of gas with radius R diffusing into a different gas with a binary diffusivity D_{12} . The time scale for the chunk to diffuse away is

$$\tau_d = R^2/D_{12}. \quad (1)$$

Now consider a spherical chunk of radius R immersed in another gas with a shear rate of $S = |\partial u/\partial y|$. The time for the chunk to distort a distance approximately equal to its diameter is the diameter divided by the velocity difference across the chunk:

$$\tau_u = 2R/2RS = 1/S. \quad (2)$$

Finally, the time for a chunk to be disrupted by a shock wave is a few times the shock passage time,

$$\tau_s = 2R/u_s, \quad (3)$$

where u_s is the shock velocity. However, we shall see that this expectation is not always fulfilled because a sufficiently weak shock may not disrupt a chunk even though some interesting fluid motions are excited by the shock passage.

The Reynolds number of the chunk is

$$\text{Re} = \frac{\rho UL}{\mu} = \frac{UL}{0.499\bar{v}\lambda}, \quad (4)$$

where U is the macroscopic flow velocity relative to the chunk, \bar{v} is the mean molecular velocity, and $L = 2R$ is the size of the chunk. Another important dimensionless parameter is the Mach number $\text{Ma} = U/c_s$, where c_s is the speed of sound. It is easy to show [14] that

$$\text{Kn} \approx 1.5\text{Ma}/\text{Re} \quad (5)$$

in cases where L is the relevant characteristic dimension.

3 Governing Equations

We shall consider several numerical experiments that illustrate how chunks are dissipated. We confine our discussion to chunks large enough for the continuum approximation to be valid. The simulations were performed with the COYOTE computational fluid dynamics program [13], which is based on the full transient multicomponent Navier-Stokes equations. The model includes a real-gas thermal equation of state, arbitrary chemical kinetics, transport coefficients from a Lennard-Jones model, a simple radiative heat loss model, and mass diffusion based on the full Stefan-Maxwell equations. Chemistry and radiation are omitted from the present calculations.

Mass conservation is expressed by the continuity equation for each species α :

$$\frac{\partial \rho_\alpha}{\partial t} + \nabla \cdot (\rho_\alpha \mathbf{u}) = -\nabla \cdot \mathbf{J}_\alpha + R_\alpha, \quad (6)$$

where ρ_α is the density of species α , \mathbf{u} is the fluid velocity, \mathbf{J}_α is the diffusional mass flux of species α , and R_α is the rate of change of species α by chemical reactions. The diffusional flux is a complex function of the flow that can be approximated in several ways that will be described shortly. The total density ρ is obtained by summing the ρ_α .

The momentum equation is

$$\frac{\partial(\rho \mathbf{u})}{\partial t} + \nabla \cdot (\rho \mathbf{u} \mathbf{u}) = \sum_{\alpha} \rho_{\alpha} \mathbf{F}_{\alpha} - \nabla P + \nabla \cdot \mathcal{S}, \quad (7)$$

where P is the pressure, and \mathbf{F}_{α} is the body force per unit mass acting on species α , which in most applications is the gravitational acceleration \mathbf{g} . Because we consider only fluids, we assume that the viscous stress tensor is

$$\begin{aligned} \mathcal{S} &= \mu \left[\nabla \mathbf{u} + (\nabla \mathbf{u})^T \right] + \mu_1 (\nabla \cdot \mathbf{u}) \mathcal{U} \\ &= \mu \left[\nabla \mathbf{u} + (\nabla \mathbf{u})^T \right] + \left(\mu_b - \frac{2\mu}{3} \right) (\nabla \cdot \mathbf{u}) \mathcal{U}, \end{aligned} \quad (8)$$

where μ is the coefficient of viscosity, μ_1 is the second coefficient of viscosity, \mathcal{U} is the unit tensor, and μ_b is the bulk viscosity. In almost all studies, the bulk viscosity is set to zero, which is correct, strictly speaking, only for perfect monatomic gases.

We choose the thermal internal energy equation to express energy conservation:

$$\frac{\partial(\rho I)}{\partial t} + \nabla \cdot (\rho I \mathbf{u}) = -P \nabla \cdot \mathbf{u} + \mathcal{S} : \nabla \mathbf{u} - \nabla \cdot \mathbf{q} + \sum_{\alpha} H_{\alpha} R_{\alpha} + \sum_{\alpha} \mathbf{F}_{\alpha} \cdot \mathbf{J}_{\alpha}, \quad (9)$$

where I is the specific thermal internal energy, \mathbf{q} is the heat flux, and H_{α} is the heat of formation of species α . Note that for $\mathbf{F}_{\alpha} = \mathbf{g}$, the last term vanishes.

Closing these equations for a multicomponent fluid requires specifying mass and heat fluxes, plus several transport coefficients. This topic is quite complex, and we shall limit our present discussion to an approximate closure that has been used for combustion applications. It is applicable to dilute, unionized gases for which Chapman-Enskog theory is a good approximation. That is, the molecular distribution functions have only small departures from Maxwellian and gradient lengths are much greater than the mean free path. The heat flux \mathbf{q} used in COYOTE is [15, 28]

$$\mathbf{q} = -K \nabla T + \sum_{\alpha} h_{\alpha}(T) \mathbf{J}_{\alpha} - \sum_{\alpha} \frac{RT}{M_{\alpha} X_{\alpha}} D_{\alpha}^T \mathbf{d}_{\alpha}, \quad (10)$$

where R is the gas constant, M_{α} is the species molecular weight, X_{α} is the species mole fraction, T is the temperature, K is the multicomponent thermal conductivity, h_{α} is the specific enthalpy of species α , D_{α}^T is the multicomponent thermal diffusion coefficient, and

$$\mathbf{d}_{\alpha} = \nabla X_{\alpha} + (X_{\alpha} - Y_{\alpha}) \frac{\nabla P}{P} - \frac{1}{P} \left[\rho_{\alpha} \mathbf{F}_{\alpha} - Y_{\alpha} \sum_{\beta} \rho_{\beta} \mathbf{F}_{\beta} \right], \quad (11)$$

where Y_α is the species mass fraction ρ_α/ρ .

The thermal equation of state is assumed to be given as the sum of the partial pressures of an ideal gas for each species. The caloric equation of state is given as the species-density-weighted sum of the species thermal internal energies, each of which is assumed to be a function only of temperature. The JANAF tables [16, 17, 18] provide a homogeneous set of thermochemical data for a large collection of materials, and these tables are used to supply the specific enthalpy and heat of formation for each species of interest. These enthalpies are easily converted into internal energies.

In the present study, we use the Lennard-Jones model to estimate the transport coefficients [19]. This model provides a viscosity (in cgs units; to get SI units, multiply the cgs viscosity by 0.1) for each species,

$$\mu_\alpha = \frac{5}{16} \left(\frac{m_H k_B}{\pi} \right)^{1/2} \frac{(M_\alpha T)^{1/2}}{\sigma_\alpha^2 \Omega_\nu} = 2.6693 \times 10^{-5} \frac{(M_\alpha T)^{1/2}}{\sigma_\alpha^2 \Omega_\nu}, \quad (12)$$

where m_H is the mass of one atomic mass unit in grams, k_B is the Boltzmann constant, σ_α is the collision diameter in Å, and Ω_ν is the collision integral approximated by

$$\Omega_\nu = 1.147 (T/T_{e\alpha})^{-0.145} + (T/T_{e\alpha} + 0.5)^{-2}, \quad (13)$$

where $T/T_{e\alpha} = T k_B/\epsilon_\alpha$ is the reduced temperature and ϵ_α is the Lennard-Jones potential well depth [20, 21]. Kee, *et al.* [15] recommend interpolation in Table V of Monchick and Mason [22], which includes dependence of the collision integral on the reduced dipole moment of the molecule, δ , as well as dependence on $T_{e\alpha}$. Equation 13 is accurate to a few percent for Monchick and Mason's $\delta < 0.5$ at low temperatures, and it becomes valid for larger values of δ at higher temperatures.

Once the species viscosities have been calculated, they must be combined to provide the viscosity of the fluid mixture. We adopt Wilke's law [23] (see also Bird *et al.* [24]). For N species,

$$\mu = \sum_{\alpha=1}^N \frac{X_\alpha \mu_\alpha}{\sum_{\beta=1}^N X_\beta \Phi_{\alpha\beta}}, \quad (14)$$

where X_α is the mole fraction of species α and where

$$\Phi_{\alpha\beta} = 8^{-1/2} \left(1 + \frac{M_\alpha}{M_\beta} \right)^{-1/2} \left[1 + \left(\frac{\mu_\alpha}{\mu_\beta} \right)^{1/2} \left(\frac{M_\beta}{M_\alpha} \right)^{1/4} \right]^2. \quad (15)$$

In the original COYOTE program, K was calculated from the mixture viscosity μ and a constant mixture Prandtl number. This capability has been expanded to allow calculation of the conductivity based on the local composition and temperature, just as was done for the viscosity. Following the procedure of Hayashi and Hishida [20], we calculate the conductivity from the viscosity using the Eucken correction, which is discussed also by Ferziger and Kaper [25] and by Hirschfelder, Curtiss, and Bird [28]:

$$K_{\alpha} = 0.25 (9\gamma_{\alpha} - 5)\mu_{\alpha} C_{v\alpha}, \quad (16)$$

where $C_{v\alpha}$ is the specific heat at constant volume and γ_i is the ratio of specific heats. Kee, *et al.* [15] describe a more complex approximation that we have not implemented. Their model accounts more accurately for the internal quantum states of the molecules.

We do not use the true multicomponent thermal conductivity, but an approximation called the “mixture averaged model” in the CHEMKIN program [15]. There are two possible mixture rules for the conductivity. The first is to use Eq. 14 with μ_{α} replaced by K_{α} , but with the same values of $\Phi_{\alpha\beta}$ as used for the mixture viscosity [24]. The second rule is due to Mathur *et al.* [26] and is recommended by Kee, *et al.* [15]:

$$K = \frac{1}{2} \left[\sum_{\alpha=1}^N X_{\alpha} K_{\alpha} + \left(\sum_{\alpha=1}^N X_{\alpha} / K_{\alpha} \right)^{-1} \right]. \quad (17)$$

We presently use the latter rule in COYOTE.

Calculation of the diffusional mass fluxes is a complicated task (for example, [24] and [27]). Many combustion studies simply use Fick’s law,

$$\mathbf{J}_{\alpha} = -\rho D_{\alpha} \nabla(\rho_{\alpha}/\rho), \quad (18)$$

where ρ is the total density, and D_{α} is the species diffusivity. The original version of COYOTE used this approximation with the same value of D_{α} for all species, and this value was given as the kinematic viscosity of the mixture divided by a constant mixture Schmidt number. This simple model has the advantages that it is easy to program, computationally inexpensive, and the species mass fluxes properly add up to zero when summed over species. Experience suggests that it is adequate for turbulent flows (where molecular transport is overwhelmed by the turbulent eddy diffusion) and in some laminar cases using global

chemical kinetics (where the detailed chemical composition is not being modeled all that accurately in any case). In cases where the flow is laminar or nearly so, or where a detailed chemical reaction network is included, a more accurate model is required.

We use a more accurate model based on the Stefan-Maxwell equations [28]

$$\sum_{\beta} (X_{\alpha} X_{\beta} / D_{\alpha\beta}) (\mathbf{u}_{\beta} - \mathbf{u}_{\alpha}) = \mathbf{G}_{\alpha} \equiv \mathbf{d}_{\alpha} + \chi_{\alpha} \nabla \ln T \quad (\alpha = 1, \dots, N), \quad (19)$$

where N is the number of species in the mixture, \mathbf{u}_{α} is the velocity of species α , X_{α} is the mole fraction of species α , and $D_{\alpha\beta}$ is the binary diffusivity for the pair of species (α, β) . The χ_{α} are related to the species thermal diffusion coefficients and will be discussed shortly. The diffusional mass fluxes are given by

$$\mathbf{J}_{\alpha} = \rho_{\alpha} (\mathbf{u}_{\alpha} - \mathbf{u}), \quad (20)$$

where \mathbf{u} is the mass-weighted mixture velocity calculated by COYOTE,

$$\rho \mathbf{u} = \sum_{\alpha} \rho_{\alpha} \mathbf{u}_{\alpha}. \quad (21)$$

The diffusional fluxes can be found by solving the coupled system 19 through 21 for each cell on each time step. This involves solving a linear system for each cell face on each cycle. The only real “trick” to doing this is to eliminate all rows of the matrix $X_{\alpha} X_{\beta} / D_{\alpha\beta}$ that are all zeroes before calling the linear system solver. The resulting matrix is still singular, so it is necessary to replace one row of the matrix with Eq. 21. We usually select the row for the least abundant species. There can still sometimes be problems with the matrix being ill-conditioned, so in practice it occasionally is necessary also to eliminate rows for species with densities less than some cutoff value, which we normally take to be zero. With very low abundances, it is usually safe to assume the diffusional velocity is zero. It seems to help to solve for $X_{\alpha} \mathbf{u}_{\alpha}$ rather than for \mathbf{u}_{α} , so the β th row of the coefficient matrix is $X_{\beta} / D_{\alpha\beta}$.

We follow Hayashi and Hishida [20] in evaluation of the binary diffusion coefficients:

$$D_{\alpha\beta} = 1.8829 \times 10^3 \frac{\left[T^3 \left(\frac{M_{\alpha} + M_{\beta}}{M_{\alpha} M_{\beta}} \right) \right]^{1/2}}{P \sigma_{\alpha\beta}^2 \Omega_D}, \quad (22)$$

$$D_{\alpha\beta} = \frac{3}{16} \left(\frac{2k_B^3}{\pi m_H} \right)^{1/2} \frac{\left[T^3 \left(\frac{M_\alpha + M_\beta}{M_\alpha M_\beta} \right) \right]^{1/2}}{P \sigma_{\alpha\beta}^2 \Omega_D} f_D = 1.8829 \times 10^3 \frac{\left[T^3 \left(\frac{M_\alpha + M_\beta}{M_\alpha M_\beta} \right) \right]^{1/2}}{P \sigma_{\alpha\beta}^2 \Omega_D}, \quad (23)$$

where P is the total pressure of the mixture and f_D is a correction factor in the range $1.0 \leq f_D \leq 1.1$. We take $f_D = 1.0$, and the numerical factor in the right equality assumes cgs units except for $\sigma_{\alpha\beta}$, which is in Ångstroms. We also use

$$\sigma_{\alpha\beta} = 0.5(\sigma_\alpha + \sigma_\beta), \quad (24)$$

$$\Omega_D = (T/T_{e\alpha\beta})^{-0.145} + (T/T_{e\alpha\beta} + 0.5)^{-2}, \quad (25)$$

and

$$T_{e\alpha\beta} = (T_{e\alpha} T_{e\beta})^{1/2}. \quad (26)$$

It is usual to ignore the thermal diffusion terms and set $\chi_\alpha = D_\alpha^T = 0$. Not only are thermal diffusion effects generally small, there are practical difficulties associated with obtaining the required values of χ_α . There is a shortage of experimental data, and the traditional theory is so complex as to hinder its application by the nonspecialist. However, Ramshaw has developed an approximate simplified theory [29, 30] that has been incorporated into COYOTE. This model is valid only for ideal gases, and we shall specialize it to the one-temperature case. The first step is to estimate the collision cross section between molecules of types α and β as

$$\sigma^{\alpha\beta} = 0.25\pi(\sigma_\alpha + \sigma_\beta)^2. \quad (27)$$

We define

$$\gamma_{\alpha\beta} = \frac{m_H}{2k_B T} \frac{M_\alpha M_\beta}{M_\alpha + M_\beta}. \quad (28)$$

With these two parameters we calculate the collision time

$$\tau_\alpha = \frac{1}{2} \left[\sum_{\beta=1}^N \frac{n_\beta \sigma^{\alpha\beta}}{(\pi \gamma_{\alpha\beta})^{1/2}} \right]^{-1}, \quad (29)$$

where n_β is the number density of species β . Next we calculate

$$\mathcal{B}_{\alpha\beta} = -\frac{RTP X_\alpha X_\beta M_\alpha \tau_\beta}{2D_{\alpha\beta} M_\beta (M_\alpha + M_\beta)}, \quad (30)$$

which are in turn used to calculate the χ_α using the left equality of

$$\chi_\alpha = P^{-1} \sum_{\beta=1}^N (\mathcal{B}_{\beta\alpha} - \mathcal{B}_{\alpha\beta}) = \sum_{\beta=1}^N \frac{X_\alpha X_\beta}{D_{\alpha\beta}} \left(\frac{D_\alpha^T}{\rho_\alpha} - \frac{D_\beta^T}{\rho_\beta} \right). \quad (31)$$

The χ_α are used in the Stefan-Maxwell equations 19, which in turn are used with equation 20 to calculate the diffusion fluxes. The second equality in equation 31 is a linear system that can be solved for the D_α^T for use in evaluating the Dufour term in the energy flux. This system is singular, and one equation must be replaced by the constraint

$$\sum_{\alpha} D_{\alpha}^T = 0. \quad (32)$$

4 Diffusion of a Stationary Sphere

The simplest problem is the diffusion of a stationary sphere of a heavy gas (in this case, xenon) into an ambient light gas (helium). We choose a temperature of 2000 K and a pressure of 10 atmospheres. The chunk radius is 12 μm . The calculations are two dimensional in cylindrical coordinates. The uniform grid has 80 by 150 zones, each 0.8 μm square.

Table 1 gives the COYOTE input file for this problem, except `vreg(1)=0.0`. The Lennard-Jones parameters for helium are $\sigma = 2.57 \text{ \AA}$ and $\epsilon/k = 10.2 \text{ K}$. The Lennard-Jones parameters for xenon are $\sigma = 3.937 \text{ \AA}$ and $\epsilon/k = 229.8 \text{ K}$. The binary diffusivity for helium and xenon at 2000 K is $D_{12} = 1.363 \text{ cm}^2/\text{s}$. This gives a diffusion time scale $\tau_d = 1.057 \mu\text{s}$. The sound speeds in the pure gases are $2.632 \times 10^5 \text{ cm/s}$ for He and $4.595 \times 10^4 \text{ cm/s}$ for Xe. The flow velocity past the Xe sphere has a Mach number of zero. The kinematic viscosities of the pure gases are $2.767 \text{ cm}^2/\text{s}$ for He and $0.1298 \text{ cm}^2/\text{s}$ for Xe. The mean free paths are approximately 0.2 μm in the He and 0.06 μm in the Xe. This gives a Knudsen number of 0.02, so this problem is safely in the continuum regime.

Figure 1 shows the mole fraction of xenon after one time step ($t = 5.0 \text{ ps}$). The left boundary is the axis of symmetry, and the other 3 boundaries are adiabatic, free-slip walls. The xenon sphere has a radius of 15 zones. It was defined by filling with xenon all zones whose centers are inside a sphere of radius 12 μm . This is why the boundary appears somewhat jagged. Figure 2 shows the contours of Xe mole fraction at $t = 0.23 \tau_d$. The f contour is half way between the extreme values of the mole fraction, and it has the same diameter as the original particle. The b contour (10 percent from `min` to `max`) is twice as big. The central (`max`) value already is down to 0.46 from 1.0. The contours are nicely circular and centered on the original center of the sphere. Figure 3 shows the Xe mole fraction at

$t = 0.46\tau_d$, and the sphere continues to grow spherically and become more diluted at the center.

Figures 4 and 5 show the Xe mass fractions at the same times as Figs. 2 and 3. The contours are much larger and the fractional dilution of the central region seems to be smaller. These features are simply the result of the large difference in the molecular weights of Xe and He.

Figures 6-8 show the velocity field at the same times as Figs. 1-3. The velocity vector at every third zone is shown in these plots. We find that the diffusion process creates a spherical expansion of the particle by advection in addition to the spreading caused by the diffusion process. It is easy to see why this must occur. The center of mass of the initial condition is on the axis, below the center of the mesh since the xenon is several times denser than the helium. In the final steady state, the fluids are uniformly mixed, and the center of mass will be at the midpoint of the axis. Since the diffusion terms cannot cause a net movement of mass, there must be a macroscopic velocity field established to allow the movement of the center of mass. It is easy to see how this motion is caused by the diffusion terms. Consider the initial condition, which has a sharp interface between the two gases. On the first time step, the diffusion fluxes mix a small mass of helium into the xenon, and the same mass of xenon into the helium. However, a larger number of helium atoms are transported than xenon atoms. The contaminated xenon now has an increased number density of atoms, and hence a higher pressure, than the contaminated helium. It is this small pressure gradient that drives the gentle expansion velocity field.

5 Subsonic Flow Past a Sphere

The COYOTE input file for this case is given in Table 1. The bottom boundary has a specified inflow, and the top boundary is a constant pressure outflow boundary. The helium is initially set with a constant flow velocity everywhere, and a stationary xenon sphere is inserted into the flow. The He initially is given a uniform flow velocity of 4.0×10^4 cm/s, which is Mach 0.15 in the He and 0.87 in the Xe. Otherwise, conditions are the same as in the previous section. The Reynolds number is 35. Figure 9 shows the initial velocity field.

Figures 10-12 show the velocity vectors, xenon mole fraction, xenon mass fraction at

the same times as Figure 2, $t = 0.23\tau_d$. By this time, the helium flow has moved 12 zones, and that is very close to how far the xenon sphere’s peak mass fraction has moved. This means the sphere accommodates very quickly to the ambient flow. At this Reynolds number, we would expect the sphere to distort as shown and not to demonstrate vortices in the wake. It is also to be expected that the lowest contour would have about the same radial extent as in the no-flow solution. At later times, the xenon blob simply continues to diffuse away while advecting along with the helium. This is shown in Figures 13-15.

6 Supersonic Flow Past a Sphere

This problem is the same as in the previous section except that the helium is initially stationary except for a Mach 1.313 shock entering from the bottom of the mesh. The Reynolds number is 82. In this case, once the shock has passed the blob, the flow around the sphere is similar to that of the subsonic case. For example, Figure 16 shows the xenon mass fraction at $t = 9.3437 \times 10^{-2} \mu s$. Compare this to the subsonic flow shown in Figure 12, which is at a comparable stage of development. The sphere distorts somewhat before it begins moving along with the helium, slightly more than in the subsonic case but not quite as much as in the higher Reynolds number cases such as those reported by Jacobs [31], Quirk and Karni [32], Haas and Sturtevant [33], and Cowperthwaite [34]. The main difference between the subsonic and shocked cases is a factor of approximately 2.5 in the time scale, which is due to the difference in the ambient flow speed. However, the shock transmitted into the sphere causes some interesting transient flow features not seen in the subsonic case, namely a pair of convergent shocks that produce a localized hot, dense spot in the xenon.

Even though the converging shocks do not affect either the integrity of the blob or its accommodation to the ambient flow, they are quite interesting. The problem was rerun with twice as many zones in each direction on a 160 by 300 grid, and the results were quite similar to the coarse-mesh solution shown in the first 16 figures. The calculation was begun with the shock wave a short distance below the blob so the shock hits the bottom of the stationary blob early in the calculation. This sends a slow shock into the blob, which runs into a weak converging wave in the interior of the blob. Meanwhile, the faster shock in the surrounding helium moves around the outside of the blob, converging on the downstream

side. Figures 17 through 19 show this phenomenon at $t = 1.7105 \times 10^{-2} \mu\text{s}$. The plots show only a part of the grid in the neighborhood of the blob. Figure 17 shows two converging waves. The smaller inner wave is a remnant of the spherical velocity field set up by the diffusion process, shown in Figure 6. Before the shock hits the blob, the velocity field set up by diffusion has an outer, somewhat faster, shell of expanding material and an inner, slower shell of a converging wave that is almost converged in Figure 17. However, this wave and the subsequent expansion wave were sufficiently weak and short-lived that there was no significant influence on the remainder of the calculation. The second wave is the larger converging shock along the outer edge of the blob, which overwhelms the weak expansion driven by the diffusion. At this time, the xenon is surrounded by high pressure helium, shown in Figure 18, which drives this larger and stronger convergent shock into the blob, beginning at the interface between the two gases. The maximum temperature at this time is 3672 K.

Figures 20 through 22 show the solution at $t = 2.4605 \times 10^{-2} \mu\text{s}$, just before the outer shock converges. Somewhat later, the converging shock produces maximum compression, and the peak temperature is somewhere in the 7000 to 8000 K range. It is difficult to state the peak value with any more precision because graphics dumps were too widely spaced. The maximum compression shown in any graphics dump is on cycle 3000, and the peak compression has already passed. Asymmetric disassembly of the hot spot from the converging shock causes further compression behind an upwardly moving shock located where helium begins to become abundant, just above the point of convergence. The maximum temperature on cycle 3000 is 6041 K, but it could have been somewhat higher between graphics dumps at cycles 2750 and 3250. On cycle 3000, the maximum pressure is 1.26×10^8 dynes/cm² and the maximum density is 2.99×10^{-2} g/cm³. This material is essentially pure Xe. Under these conditions, ionization begins to be important in the xenon, and that was not included in the calculation. Calculations show that at 6000 K and the maximum pressure on cycle 3000, approximately 0.8 percent of the Xe is singly ionized. Neglect of ionization is, therefore, marginally justified in the present calculations. However, at higher temperatures and pressures, it will be necessary to include ionization. More generally, neglect of this kind of unexpected flow feature can lead to apparent composition anomalies in the case of more

complex chemistry, such as occurs in combustion.

This small, short-lived region of high compression then decays, exciting some acoustic waves that have little influence on the further evolution of the blob. The middle of the rebound is shown in Figures 29 through 34 at $t = 3.2105 \times 10^{-2} \mu\text{s}$. By the time the rebound ends, the shock has gone out of the top of the grid, and the blob is moving downstream along with the helium similar to the subsonic case. There is an indication of a stronger vortical motion on the downstream side of the blob, but this will have to be tested with additional calculations that go farther out in time and keep the blob farther away from the influence of the outflow boundary at the top of the grid.

7 Conclusion

We have performed direct numerical simulations (DNS) of a small ($24 \mu\text{m}$ diameter) xenon sphere immersed in helium, with various initial velocity differences between the two materials. This preliminary study demonstrates several things.

1. We used direct solution of the Stefan-Maxwell equations for the mass diffusion fluxes within a multidimensional finite difference computational fluid dynamics program based on the multicomponent Navier-Stokes equations. Although this approach can be algebraically simplified for the binary mixture used in the present study, the full algorithm has been used in test problems with as many as 21 species and is quite practical for much more complex mixtures.
2. Molecular transport is important for small particles and filaments. Spheres in the size range of tens of micrometers dissipate on time scales of a microsecond at temperatures typical of combustion systems. The time scale will be even shorter in the much hotter conditions typically found in ICF plasmas.
3. This approach may be extended to study the details of the dissipation of turbulent fluctuations down to the turbulence dissipation scale, hopefully providing insight and databases for developing improved closure approximations for LES.
4. In the limit of sufficiently small particles, such as we have studied here, the particles

quickly adjust to move with the local ambient gas velocity. Except for some streaming into the wake early on and some deformation of the sphere, the final dissolution of the particle is dominated by the diffusion process for all flow speeds considered. The process is roughly spherically symmetric in a reference frame moving with the particle. This observation may be helpful in developing closure approximations for the decay of composition fluctuations for a LES model.

5. The particle undergoes significant diffusion sufficiently rapidly that it makes no sense to model it with an interface between the two gases. Furthermore, it would not be appropriate to model a large system with many particles with either a particle model or a multiphase model. There is simply too large a fraction of the particle's mass mixed with helium at the molecular level for concepts such as a particle radius or an interface to be meaningful.
6. Future work should include redoing these simulations with a taller mesh or moving the calculations into a reference frame in which the ambient medium is stationary. This would allow us to follow the blobs to later times. Allowance should be made for ionization, which can be done easily with COYOTE's chemistry package. Then we should vary the conditions of the calculation, including blob radius, temperature, pressure, and Mach number of the flow. Some problems should be run in three dimensions.

8 Acknowledgments

I thank John Ramshaw for many helpful discussions on transport theory and for his comments on the manuscript. This work was performed under the auspices of the U. S. Department of Energy and the Lawrence Livermore National Laboratory under contract number W-7405-ENG-48.

References

- [1] N. A. Tahir and D. H. H. Hoffmann, "Development of advanced fuel inertial fusion targets," *Laser and Particle Beams* **15**, 575 (1997).

- [2] R. L. McCrory, L. Montierth, R. L. Morse, and C. P. Verdon, “Nonlinear evolution of ablation-driven Rayleigh-Taylor instability,” *Phys. Rev. Lett.* **46**, 336 (1981).
- [3] C. P. Verdon, R. L. McCrory, R. L. Morse, G. R. Baker, D. I. Meiron, and S. A. Orszag, “Nonlinear effects of multifrequency hydrodynamic instabilities on ablatively accelerated thin shells,” *Phys. Fluids* **25**, 1653 (1982).
- [4] H. Nishimura, H. Takabe, K. Mima, F. Hattori, H. Hasegawa, H. Azechi, M. Nakai, K. Kondo, T. Norimatsu, Y. Izawa, C. Yamanaka, and S. Nakai, “Hydrodynamic instability in an ablatively imploded target irradiated by high power green lasers,” *Phys. Fluids* **31**, 2875 (1988).
- [5] E. N. Avrorin, V. A. Lykov, V. E. Chernyakov, A. N. Shushlebin, K. A. Mustafin, V. D. Frolov, M. Yu. Kozmanov, Ya. Z. Kandiev, and A. A. Sofronov, “Computational optimization of indirect-driven targets for ignition and the engineering test facility,” *Laser and Particle Beams* **15**, 145 (1997).
- [6] E. M. Campbell, N. C. Holmes, S. B. Libby, B. A. Remington, and E. Teller, “The evolution of high-energy-density physics: From nuclear testing to the superlasers,” *Laser and Particle Beams* **15**, 607 (1997).
- [7] R. Everson, D. Manin, and L. Sirovich, “Quantification of mixing and mixing rate from experimental observations,” *AIAA J.* **36**, 121 (1998).
- [8] L. D. Cloutman and M. F. Wehner, “Numerical simulation of Richtmyer-Meshkov instabilities,” *Phys. Fluids A* **4**, 1821 (1992).
- [9] C. W. Hirt and B. D. Nichols, “Volume of fluid (VOF) method for the dynamics of free boundaries,” *J. Comput. Phys.* **39**, 201 (1981).
- [10] J. K. Dukowicz, “A particle-fluid numerical model for liquid sprays,” *J. Comput. Phys.* **35**, 229 (1980).
- [11] L. D. Cloutman, J. K. Dukowicz, J. D. Ramshaw, and A. A. Amsden, “CONCHAS-SPRAY: A Computer Code for Reactive Flows with Fuel Sprays,” Los Alamos National Laboratory report LA-9294-MS, 1982.

- [12] T. D. Butler, L. D. Cloutman, J. K. Dukowicz, and J. D. Ramshaw, "Toward a Comprehensive Model for Combustion in a Direct-Injection Stratified-Charge Engine," in *Combustion Modeling in Reciprocating Engines* (1980), Ed. J. N. Mattavi and C. A. Amann (Plenum, NY).
- [13] L. D. Cloutman, "COYOTE: A Computer Program for 2-D Reactive Flow Simulations," Lawrence Livermore National Laboratory report UCRL-ID-103611, 1990.
- [14] E. R. G. Eckert and R. M. Drake, Jr., *Analysis of Heat and Mass Transfer* (McGraw-Hill, New York, 1972).
- [15] R. J. Kee, G. Dixon-Lewis, J. Warnatz, M. E. Coltrin, and J. A. Miller, "A Fortran Computer Code Package for the Evaluation of Gas-Phase Multicomponent Transport Properties," Sandia National Laboratories report SAND86-8246, 1986; reprinted 1995.
- [16] D. R. Stull and H. Prophet, "JANAF Thermochemical Tables, 2nd ed.," U. S. Department of Commerce/National Bureau of Standards report NSRDS-NBS 37, 1971.
- [17] M. W. Chase, J. L. Curnutt, A. T. Hu, H. Prophet, A. N. Syverud, and L. C. Walker, "JANAF Thermochemical Table, 1974 Supplement," *J. Phys. Chem. Ref. Data* **3**, 311 (1974).
- [18] M. W. Chase, Jr., C. A. Davies, J. R. Downey, Jr., D. J. Frurip, M. A. McDonald, and A. N. Syverud, "JANAF Thermochemical Tables, Third Edition, Parts I and II," Supplement No. 1, *J. Phys. Chem. Ref. Data* **14** (1985).
- [19] L. D. Cloutman, "A Database of Selected Transport Coefficients for Combustion Studies," Lawrence Livermore National Laboratory report UCRL-ID-115050, 1993.
- [20] A. K. Hayashi and M. Hishida, "Numerical Study on Pulsed Jet Combustion," in *Fourth International Symposium on Computational Fluid Dynamics, Vol. III*, University of California at Davis (1991), pp. 19-24.
- [21] F. M. White, *Viscous Fluid Flow* (McGraw-Hill, New York, 1974).

- [22] L. Monchick and E. A. Mason, “Transport properties of polar gases,” *J. Chem. Phys.* **35**, 1676 (1961).
- [23] C. R. Wilke, “A Viscosity Equation for Gas Mixtures,” *J. Chem. Phys.* **18**, 517 (1950).
- [24] R. B. Bird, W. E. Stewart, and E. N. Lightfoot, *Transport Phenomena* (Wiley, New York, 1960).
- [25] J. H. Ferziger and H. G. Kaper, *Mathematical Theory of Transport Processes in Gases* (North-Holland, Amsterdam, 1972).
- [26] S. Mathur, P. K. Tondon, and S. C. Saxena, “Thermal conductivity of binary, ternary, and quaternary mixtures of rare gases,” *Mol. Phys.* **12**, 569 (1967).
- [27] S. Chapman and T. G. Cowling, *The Mathematical Theory of Non-Uniform Gases* (Cambridge University Press, London, 1952).
- [28] J. O. Hirschfelder, C. F. Curtiss, and R. B. Bird, *Molecular Theory of Gases and Liquids* (Wiley, New York, 1964).
- [29] J. D. Ramshaw, “Hydrodynamic theory of multicomponent diffusion and thermal diffusion in multitemperature gas mixtures,” *J. Non-Equilib. Thermodyn.* **18**, 121 (1993).
- [30] J. D. Ramshaw, “Simple approximation for thermal diffusion in gas mixtures,” *J. Non-Equilib. Thermodyn.* **21**, 99 (1996).
- [31] J. W. Jacobs, “The dynamics of shock accelerated light and heavy gas cylinders,” *Phys. Fluids A* **5**, 2239 (1993).
- [32] J. J. Quirk and S. Karni, “On the dynamics of a shock-bubble interaction,” *J. Fluid Mech.* **318**, 129 (1996).
- [33] J.-F. Haas and B. Sturtevant, “Interaction of weak shock waves with cylindrical and spherical gas inhomogeneities,” *J. Fluid Mech.* **181**, 41 (1987).
- [34] N. Cowperthwaite, “The interaction of a plane shock and a dense spherical inhomogeneity,” *Physica D* **37**, 264 (1989).

Table 1.
COYOTE Input File

Base Case Input (cgs units)
<pre> &coydat ncyc=0, nclast=50000, ncfilm=25000, tclast=2.41825d-06, printv=2.41825d-07, lpr=1, idebug=0, xlam0=0., xlamfl=0., nsubzx=1, izxtype(1)=1, subzxl(1)=0.00, subzxr(1)=6.4d-03, noxz(1)=81, subdxl(1)=0.1, nsubzy=1, izytype(1)=1, subzyl(1)=0., subzyr(1)=12.d-03, noyz(1)=151, subdyl(2)=0.1, alpha=0.02, beta=0.98, dtmax=-5.0e-11, deltt=5.e-12, autot=1., cyl=1., kr=1, kl=1, kb=6, kt=5, epsp=1.e-08, airmu=0., rhoad=1., ndtits=40, dtratt=1.005, gx=0., gy=0., patmt=1.013d+07, patmr=1.013d+06, patml=1.013d+06, patmb=1.013d+06, keps=0, algsgrs=0., atke=0.117, dtke=1.4, charl=0., charlf=0., cbuoy=0., lrect=1, xnumol=0., swrl=0., charlg=3.75, cbscat=0., scmol=0.7, scsgs=0.7, prmol=0.7, prsgs=0.7, tcut=700., tcute=1200., itptype=2, lwr=0, twr=300., kpoutt=3, lwt=0, lwl=0, lwb=0, tvflag=1., nregn=2, ispec1=0, is(1)=1, ie(1)=82, js(1)=1, je(1)=152, treg(1)=2000., rhoreg(1,1)=2.43835d-04, rhoreg(1,2)=0.d-04, ureg(1)=0., vreg(1)=4.d+04, omgreg(1)=0., tkereg(1)=0.d+06, epsreg(1)=0., is(2)=1, ie(2)=20, js(2)=10, je(2)=74, treg(2)=2000., rhoreg(2,1)=0.0d-05, rhoreg(2,2)=7.99807d-03, ureg(2)=0., vreg(2)=0.d+04, omgreg(2)=0., tkereg(2)=0.d+06, epsreg(2)=0., xcen(2)=0.d+00, ycen(2)=3.8d-03, radius(2)=1.2d-03, nobs=0, nsp=2, eosform(1)=2., eosform(2)=2., &end &tranco mixvis=2, jtdiff=3, jtco=11, jtco2=4, jth2o=5, jdradv=1, jdrflg=2, jdrsm=1, jdrdbg=0, &end &chemin nre=0, nrk=0, ntaps=0, printt=1.05, kwiqeq=2, jchem=1, &end </pre>

X_2 cycle= 1 $t = 5.000000D-12$ $dt = 5.000000D-12$
 max = 1.000000D+00 min = 0.000000D+00 dq = 1.000000D-01

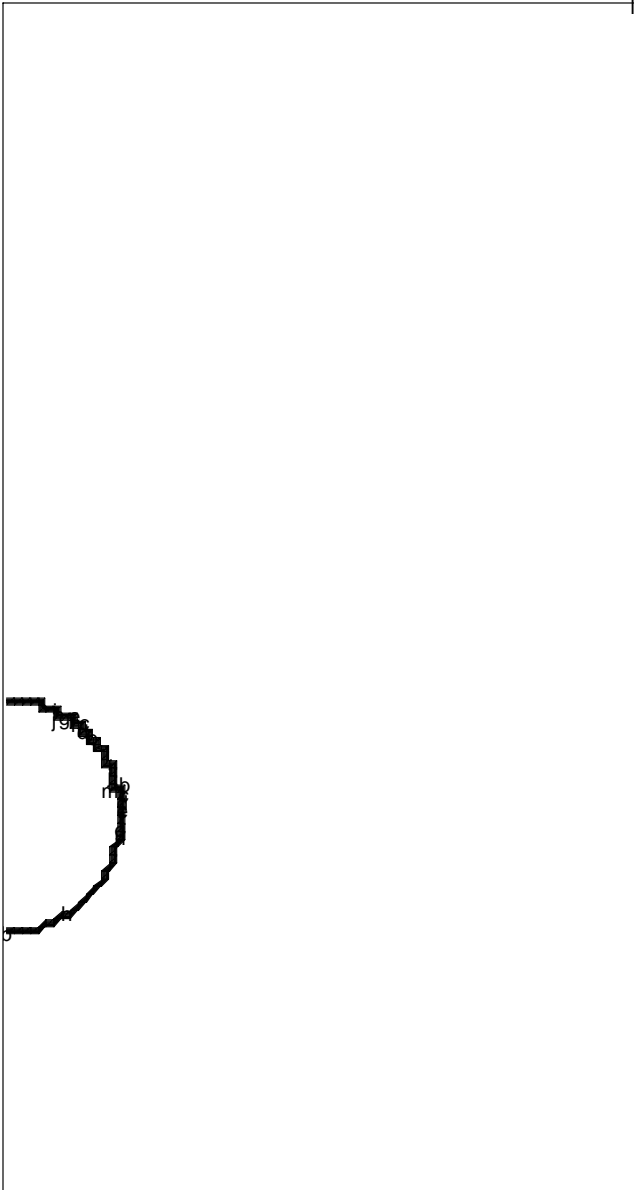


Figure 1: Xenon mole fractions for the pure diffusion case described in Section 4 at $t = 5.0$ ps.

**X 2 cycle= 5120 t= 2.418716D-07 dt= 5.000000D-11
max = 4.625416D-01 min = 2.124331D-29 dq = 4.625416D-02**

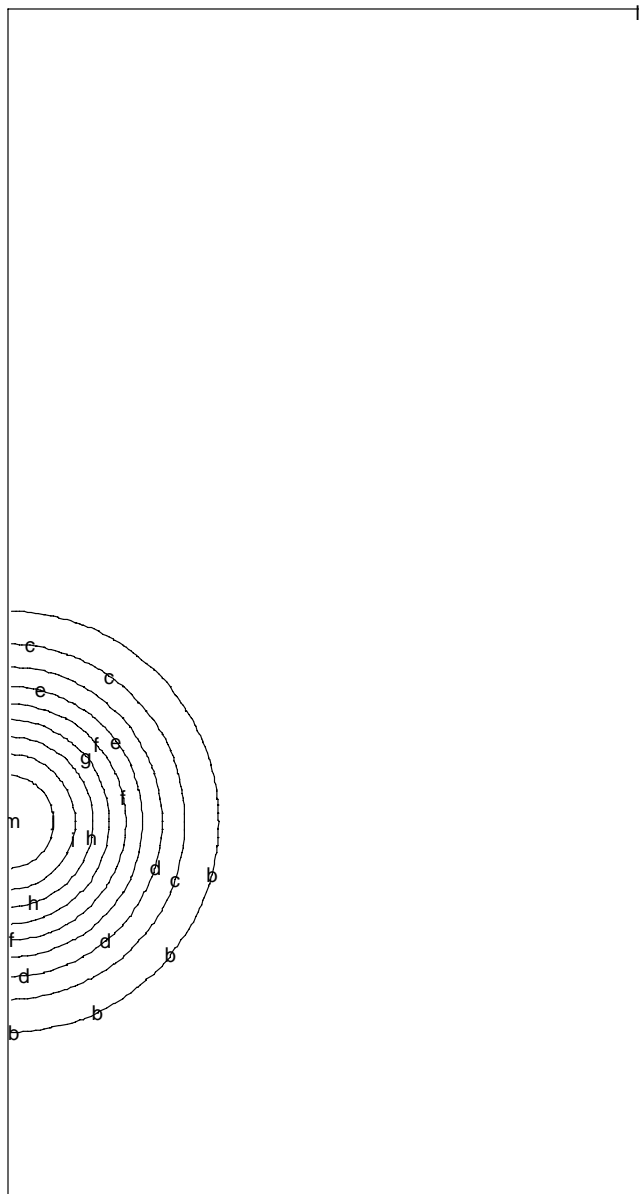


Figure 2: Xenon mole fractions for the pure diffusion case described in Section 4 at $t = 0.24187 \mu\text{s}$.

**X 2 cycle= 9956 t= 4.836716D-07 dt= 5.000000D-11
max = 2.198352D-01 min = 3.094966D-16 dq = 2.198352D-02**

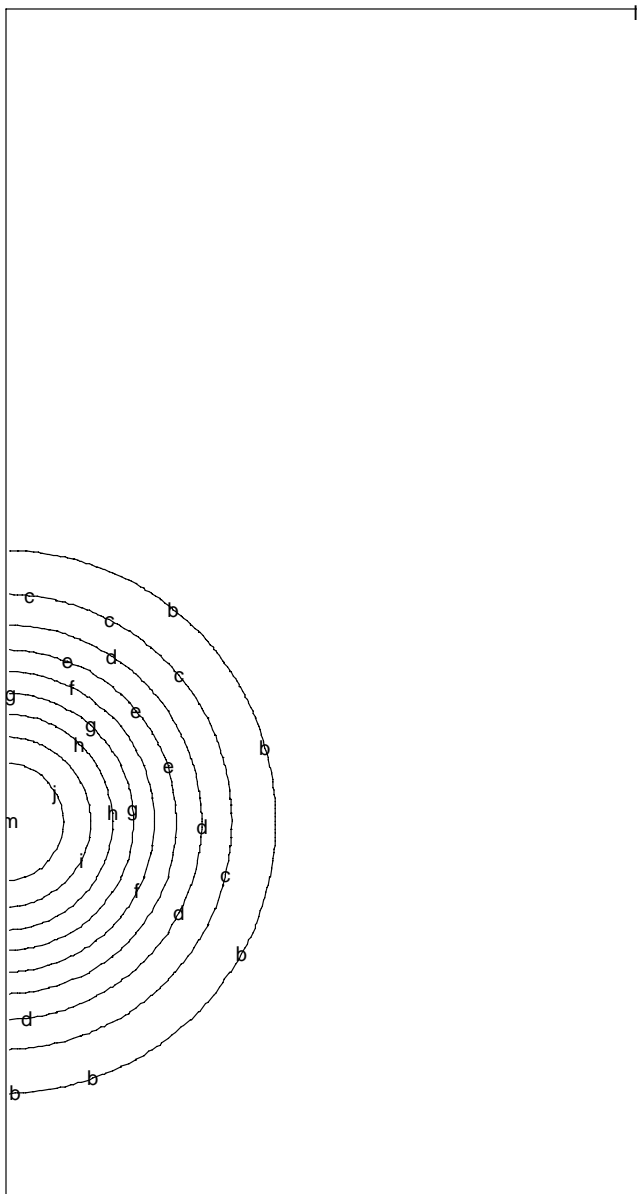


Figure 3: Xenon mole fractions for the pure diffusion case described in Section 4 at $t = 0.48367 \mu\text{s}$.

Y 2 cycle= 5120 t= 2.418716D-07 dt= 5.000000D-11
max = 9.657874D-01 min = 6.968056D-28 dq = 9.657874D-02

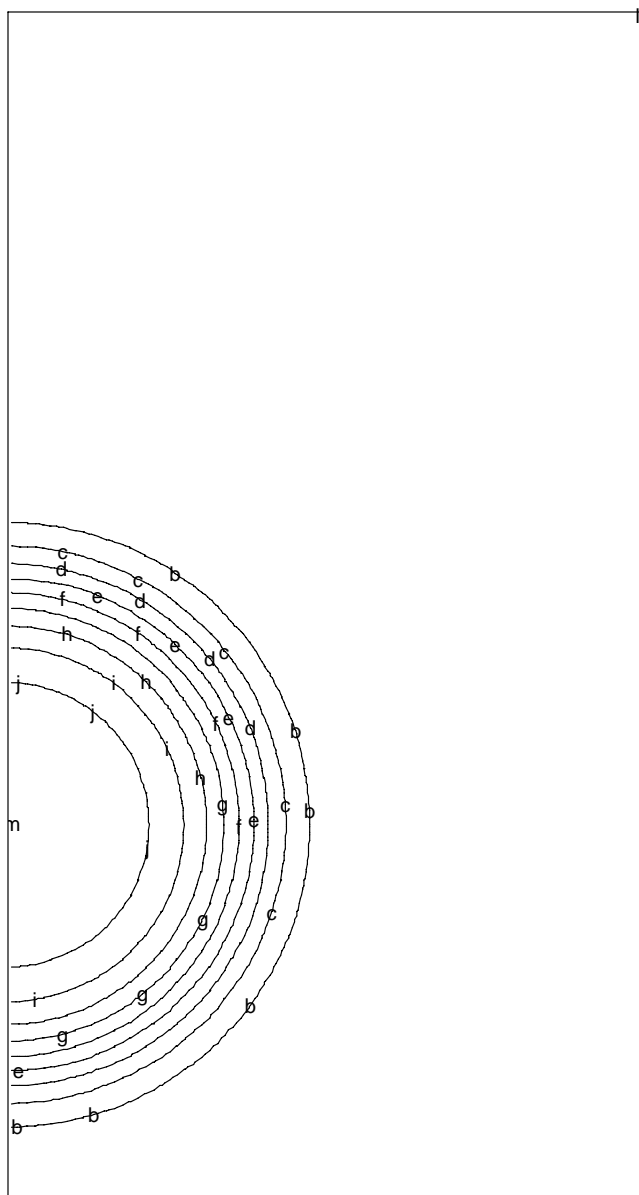


Figure 4: Xenon mass fractions for the pure diffusion case described in Section 4 at $t = 0.24187 \mu\text{s}$.

Y 2 cycle= 9956 t= 4.836716D-07 dt= 5.000000D-11
max = 9.023698D-01 min = 1.015186D-14 dq = 9.023698D-02

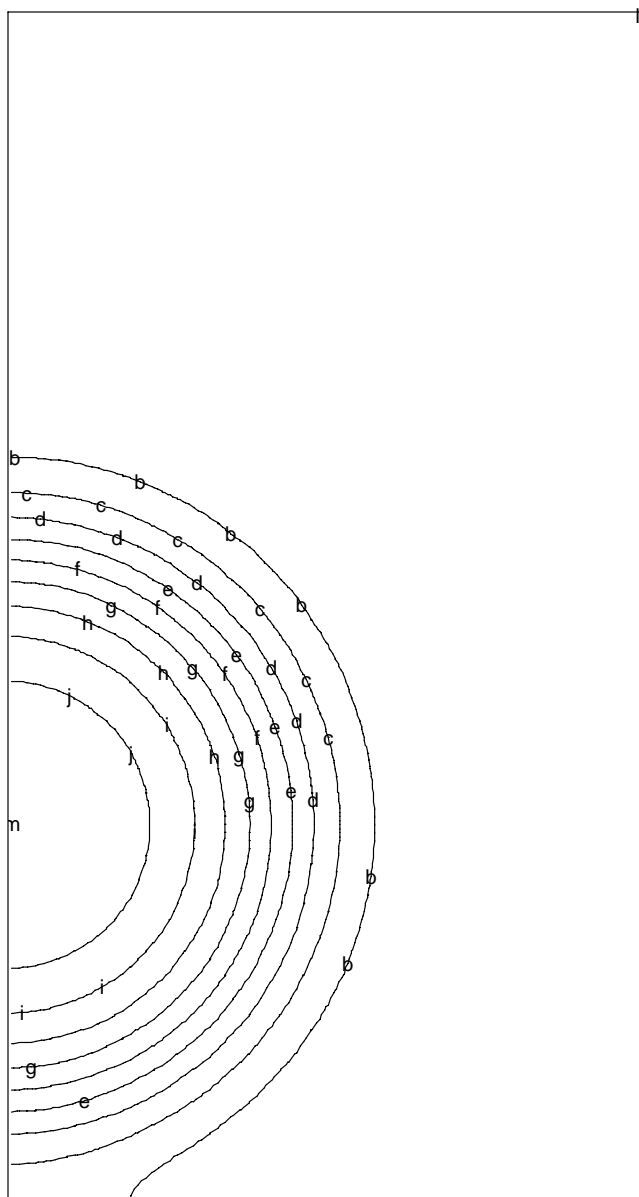


Figure 5: Xenon mass fractions for the pure diffusion case described in Section 4 at $t = 0.48367 \mu\text{s}$.

Cell center indices 2- 81, 2- 151
vel cycle = 1 vmax = 7.5222D-05

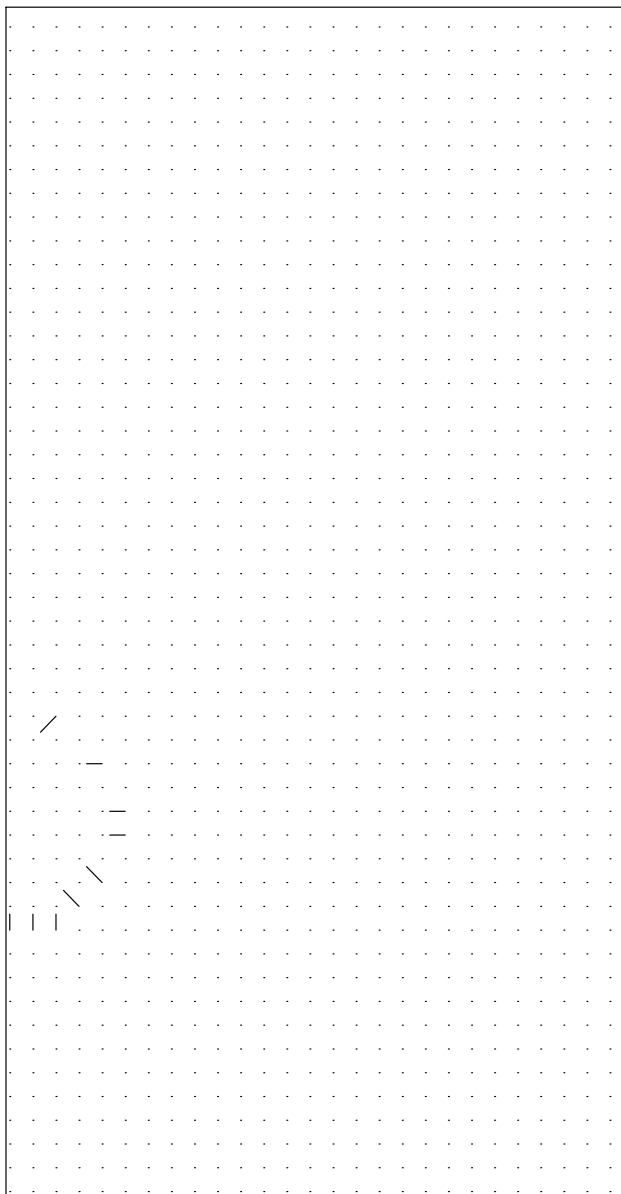


Figure 6: Velocity vectors for the pure diffusion case described in Section 4 at $t = 5.0$ ps.

Cell center indices 2- 81, 2- 151
vel cycle = 5120 vmax = 1.7187D+03

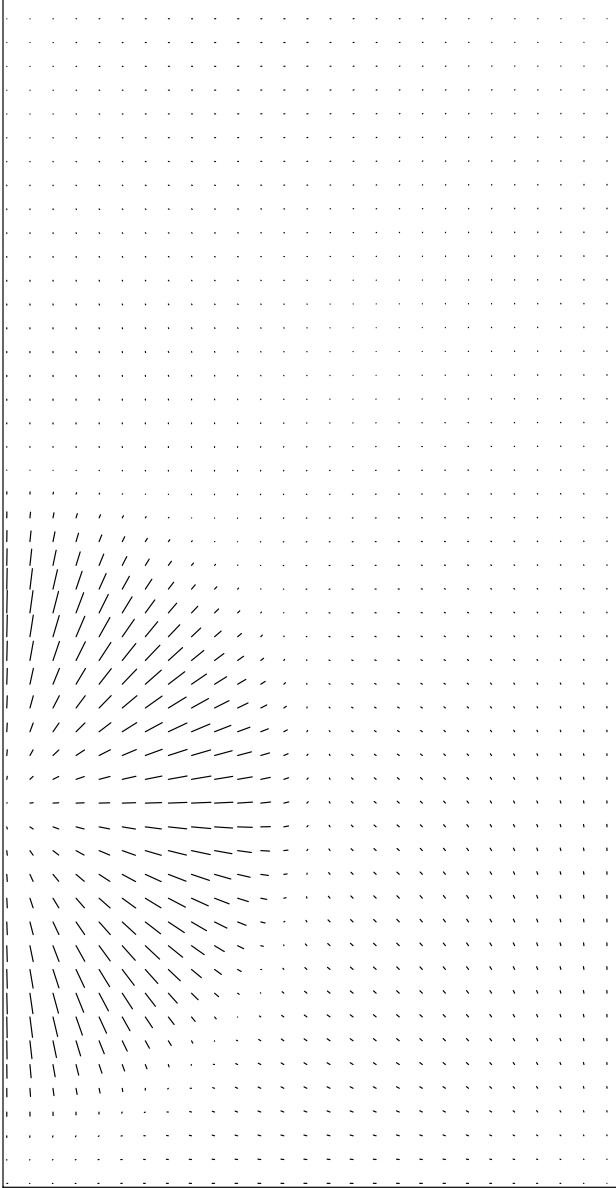


Figure 7: Velocity vectors for the pure diffusion case described in Section 4 at $t = 0.24187 \mu s$.

Cell center indices 2- 81, 2- 151
vel cycle = 9956 vmax = 1.2262D+03

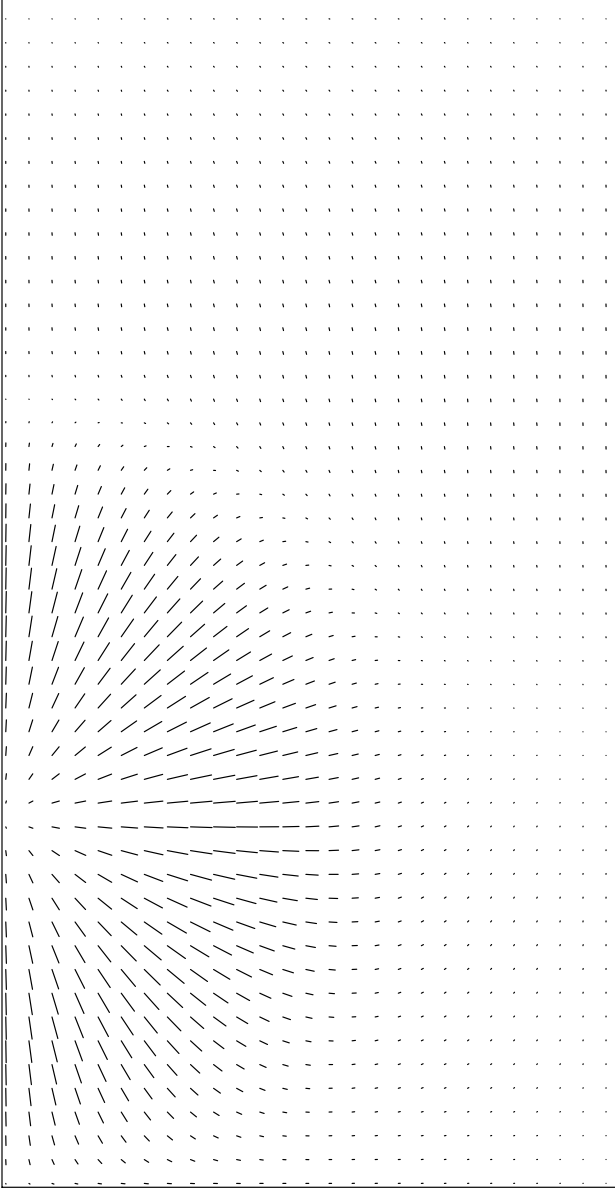


Figure 8: Velocity vectors for the pure diffusion case described in Section 4 at $t = 0.48367 \mu\text{s}$.

Cell center indices 2- 81, 2- 151
vel cycle = 1 vmax = 4.0000D+04

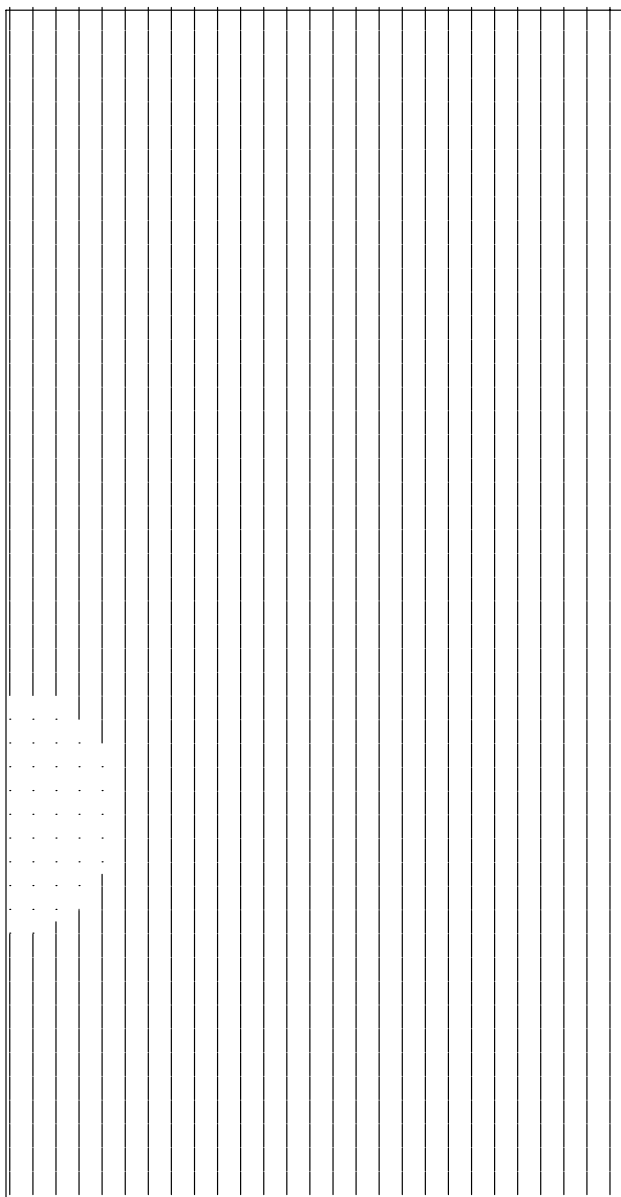


Figure 9: Velocity vectors for the subsonic coflow case described in Section 5 at $t = 5.0$ ps.

Cell center indices 2- 81, 2- 151
vel cycle = 5120 vmax = 4.8033D+04

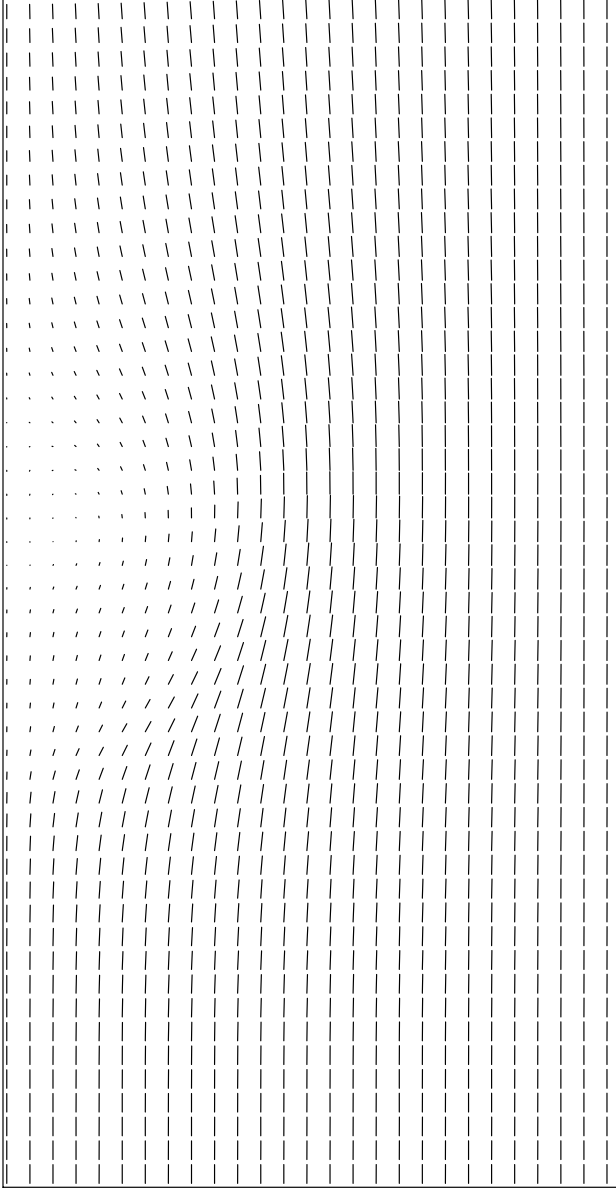


Figure 10: Velocity vectors for the subsonic coflow case described in Section 5 at $t = 0.24187 \mu s$.

X 2 cycle= 5120 t= 2.418716D-07 dt= 5.000000D-11
max = 3.767202D-01 min = -4.709927D-12 dq = 3.767202D-02

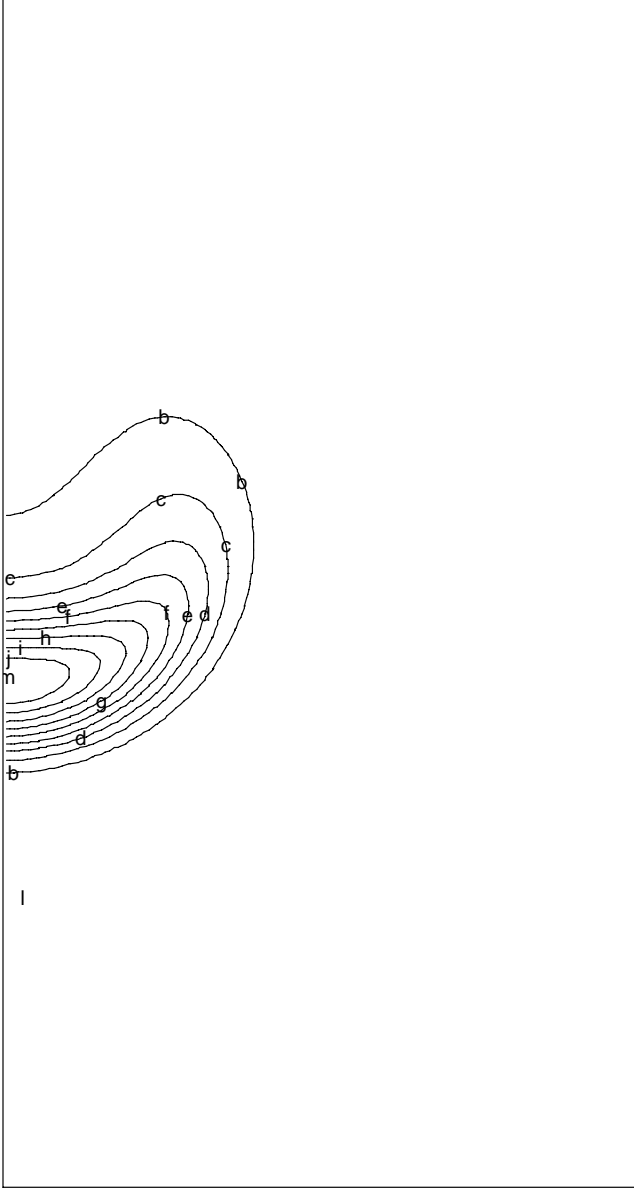


Figure 11: Xenon mole fractions for the subsonic coflow case described in Section 5 at $t = 0.24187 \mu\text{s}$.

Y 2 cycle= 5120 t= 2.418716D-07 dt= 5.000000D-11
max = 9.519821D-01 min = -1.544912D-10 dq = 9.519821D-02

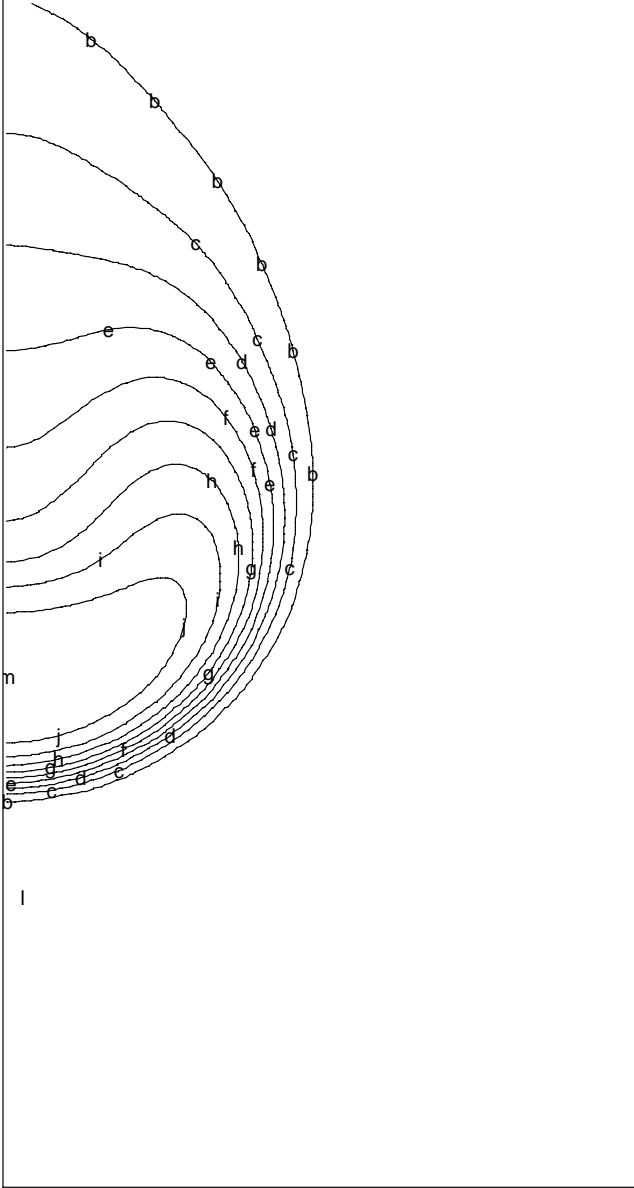


Figure 12: Xenon mass fractions for the subsonic coflow case described in Section 5 at $t = 0.24187 \mu\text{s}$.

Cell center indices 2- 81, 2- 151
vel cycle = 9956 vmax = 4.6340D+04

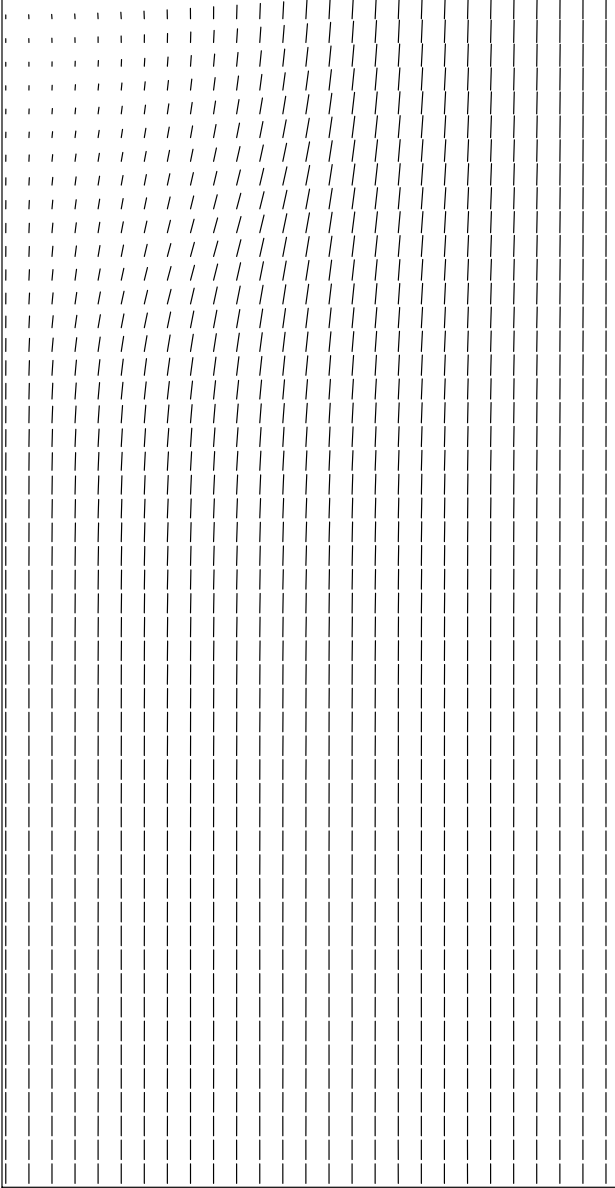


Figure 13: Velocity vectors for the subsonic coflow case described in Section 5 at $t = 0.48367 \mu s$.

X 2 cycle= 9956 t= 4.836716D-07 dt= 5.000000D-11
max = 7.381803D-02 min = -3.312770D-15 dq = 7.381803D-03

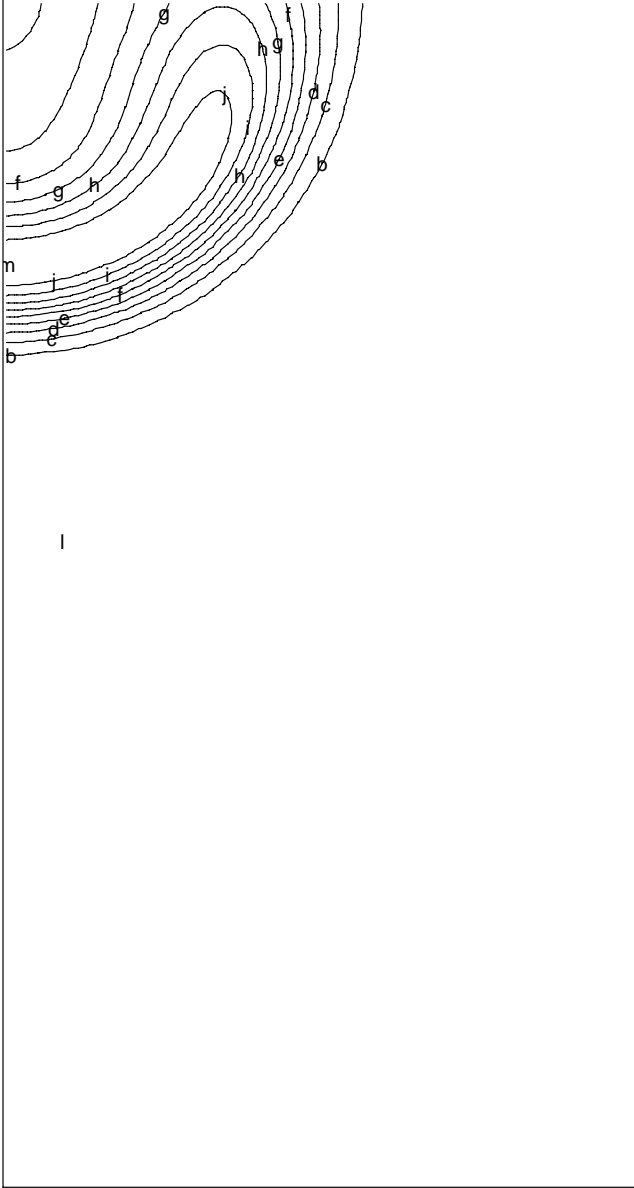


Figure 14: Xenon mole fractions for the subsonic coflow case described in Section 5 at $t = 0.48367 \mu\text{s}$.

Y 2 cycle= 9956 t= 4.836716D-07 dt= 5.000000D-11
max = 7.233213D-01 min = -1.086628D-13 dq = 7.233213D-02

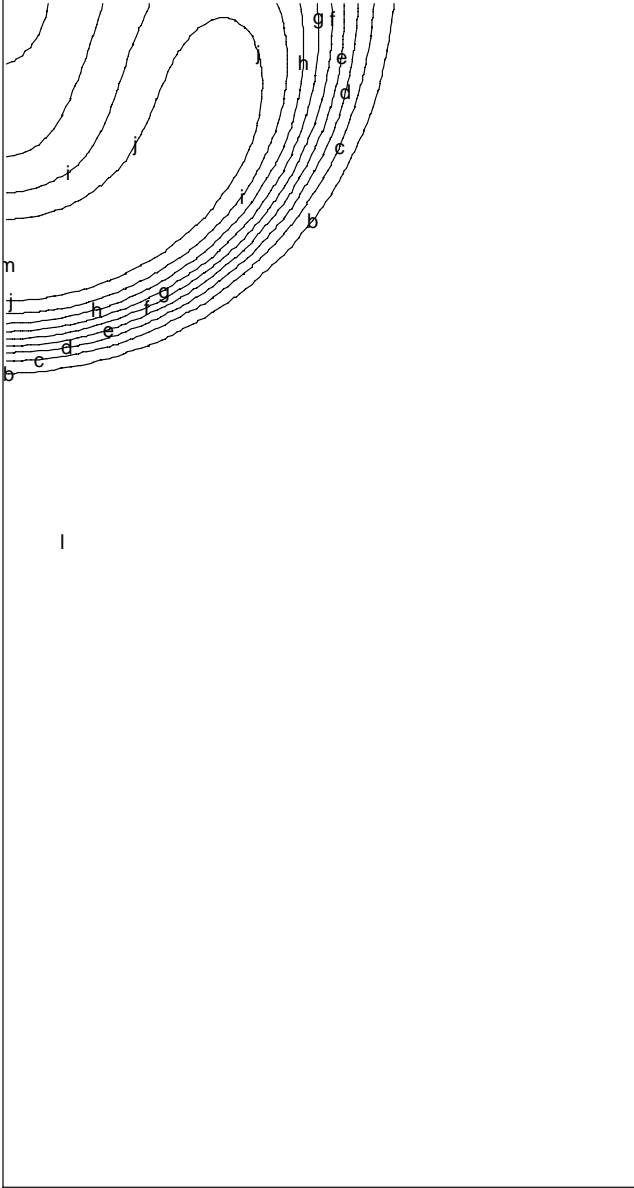


Figure 15: Xenon mass fractions for the subsonic coflow case described in Section 5 at $t = 0.48367 \mu\text{s}$.

Y 2 cycle= 5000 t= 9.343665D-08 dt= 5.000000D-11
max = 9.908268D-01 min = -3.784019D-03 dq = 9.946108D-02

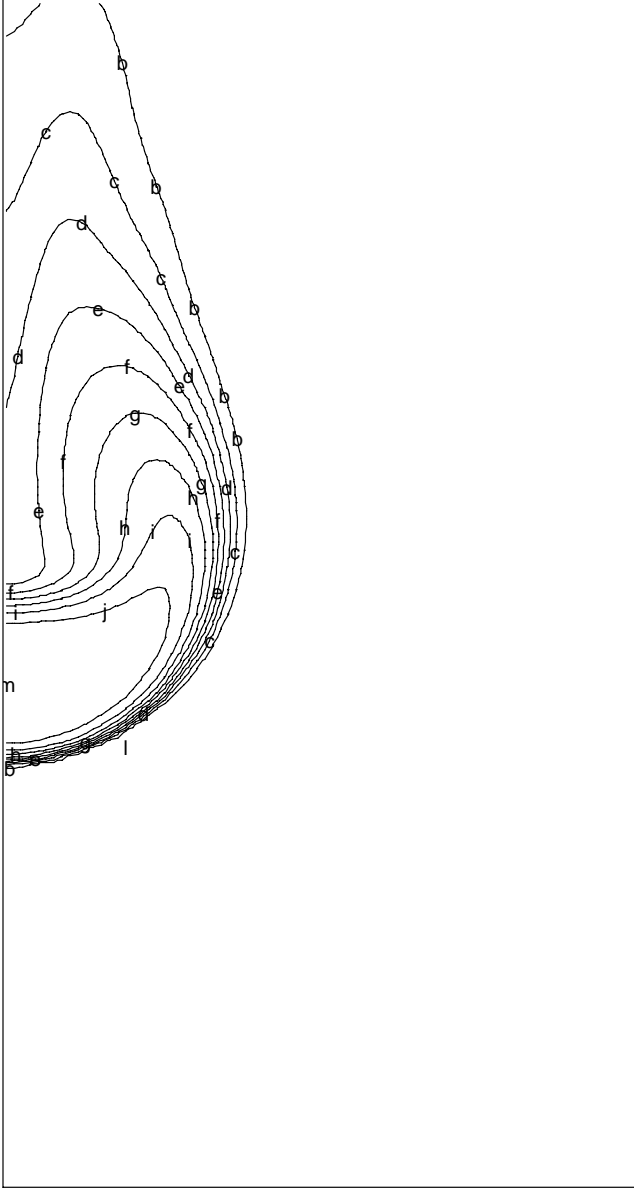


Figure 16: Xenon mass fractions for the supersonic coflow case described in Section 6 at $t = 9.3437 \times 10^{-2} \mu s$.

Cell center indices 2- 80, 70- 160
vel cycle = 1750 vmax = 1.3545D+05

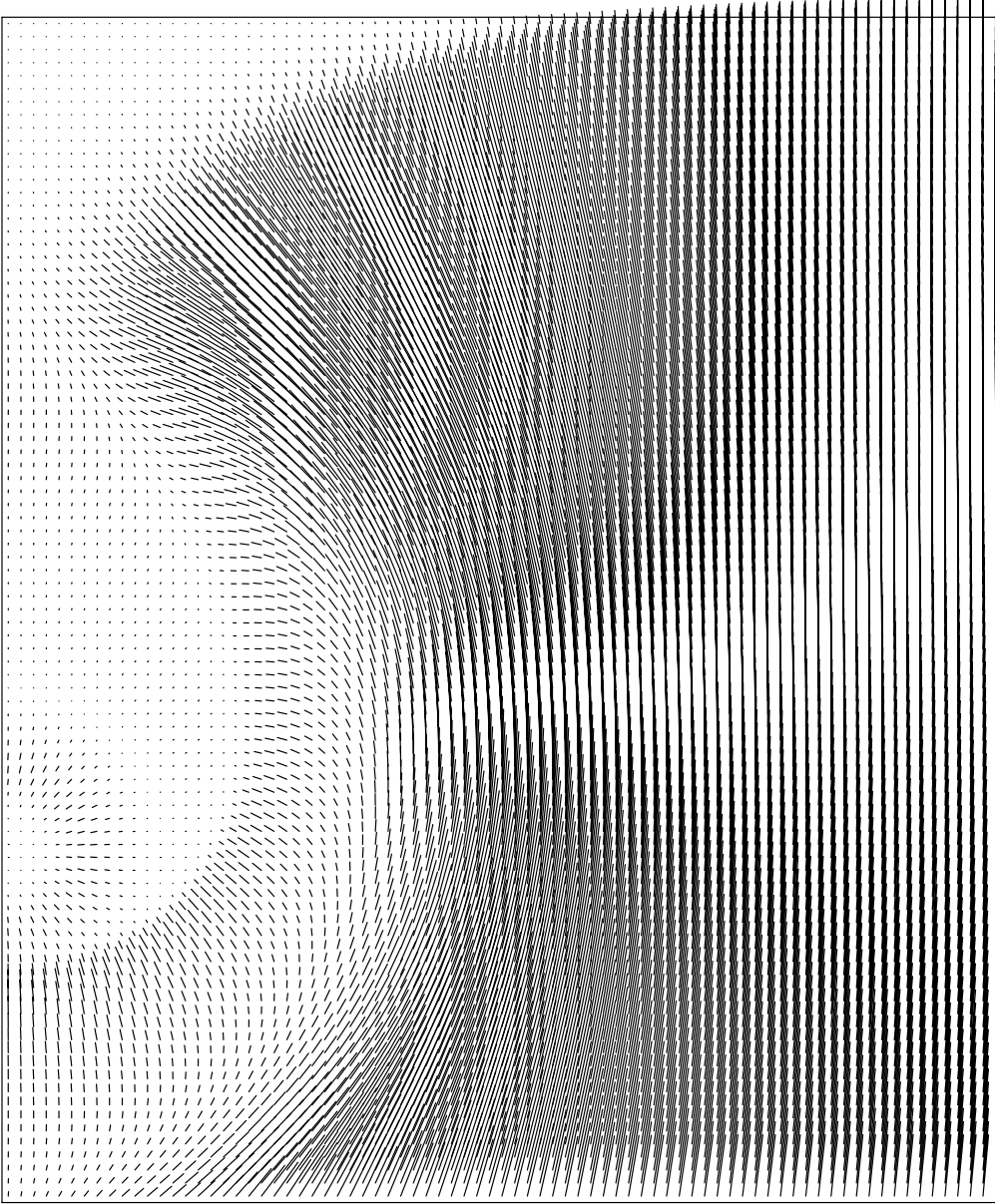


Figure 17: Velocity vectors for the supersonic coflow case described in Section 6 at $t = 1.7105 \times 10^{-2} \mu s$. The remainder of the figures cover zones 2-80 by 70-160 of the fine mesh solution. The small first converging shock is seen inside the larger, early phase of the second converging shock.

Pressure cycle= 1750 t= 1.710524D-08 dt= 1.000000D-11
max = 4.371683D+07 min = 1.013049D+07 dq = 3.358634D+06

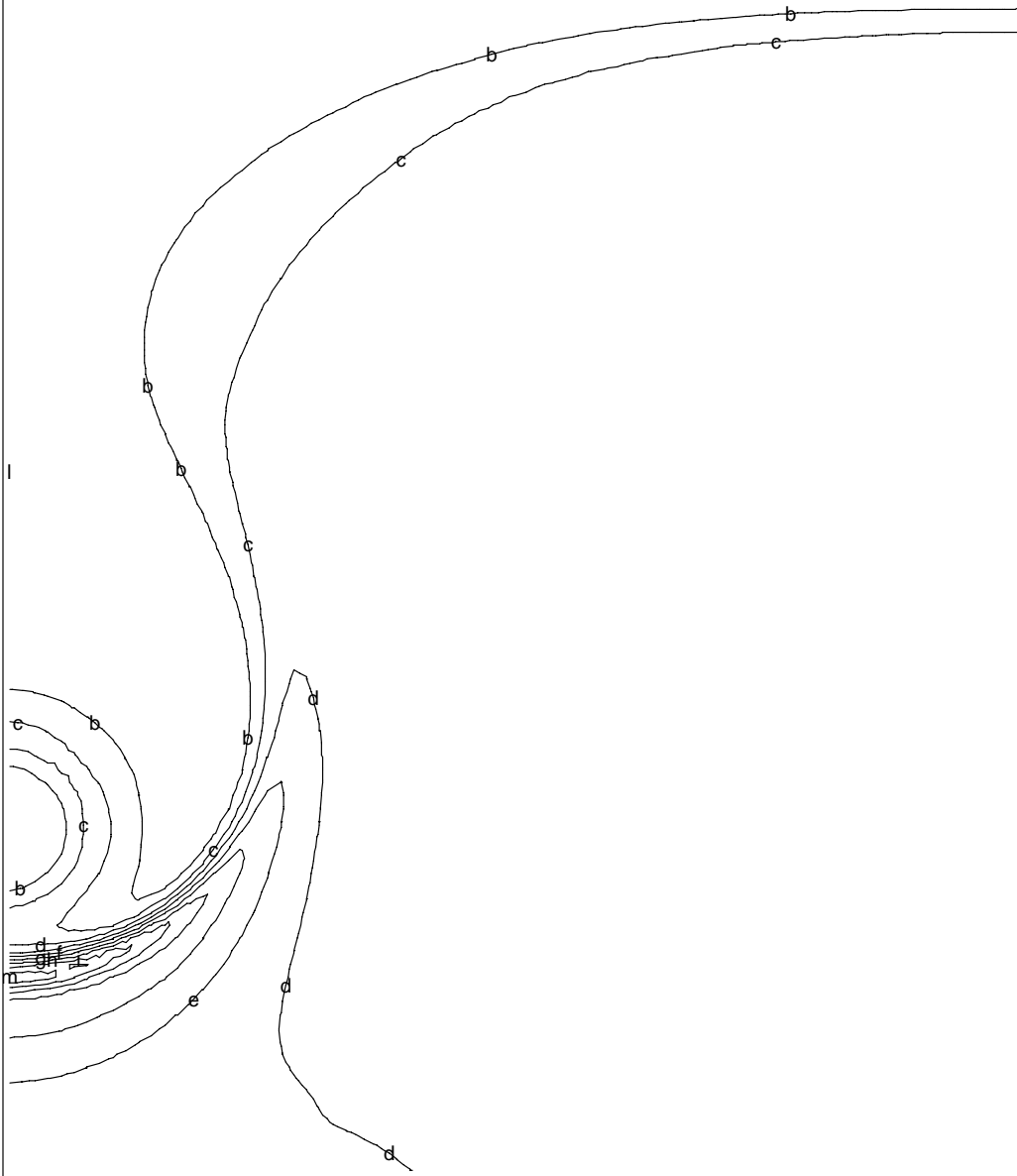


Figure 18: Pressure contours for the supersonic coflow case described in Section 6 at $t = 1.7105 \times 10^{-2} \mu s$.

Y 2 cycle= 1750 t= 1.710524D-08 dt= 1.000000D-11
max = 9.999998D-01 min = -4.160029D-07 dq = 1.000000D-01

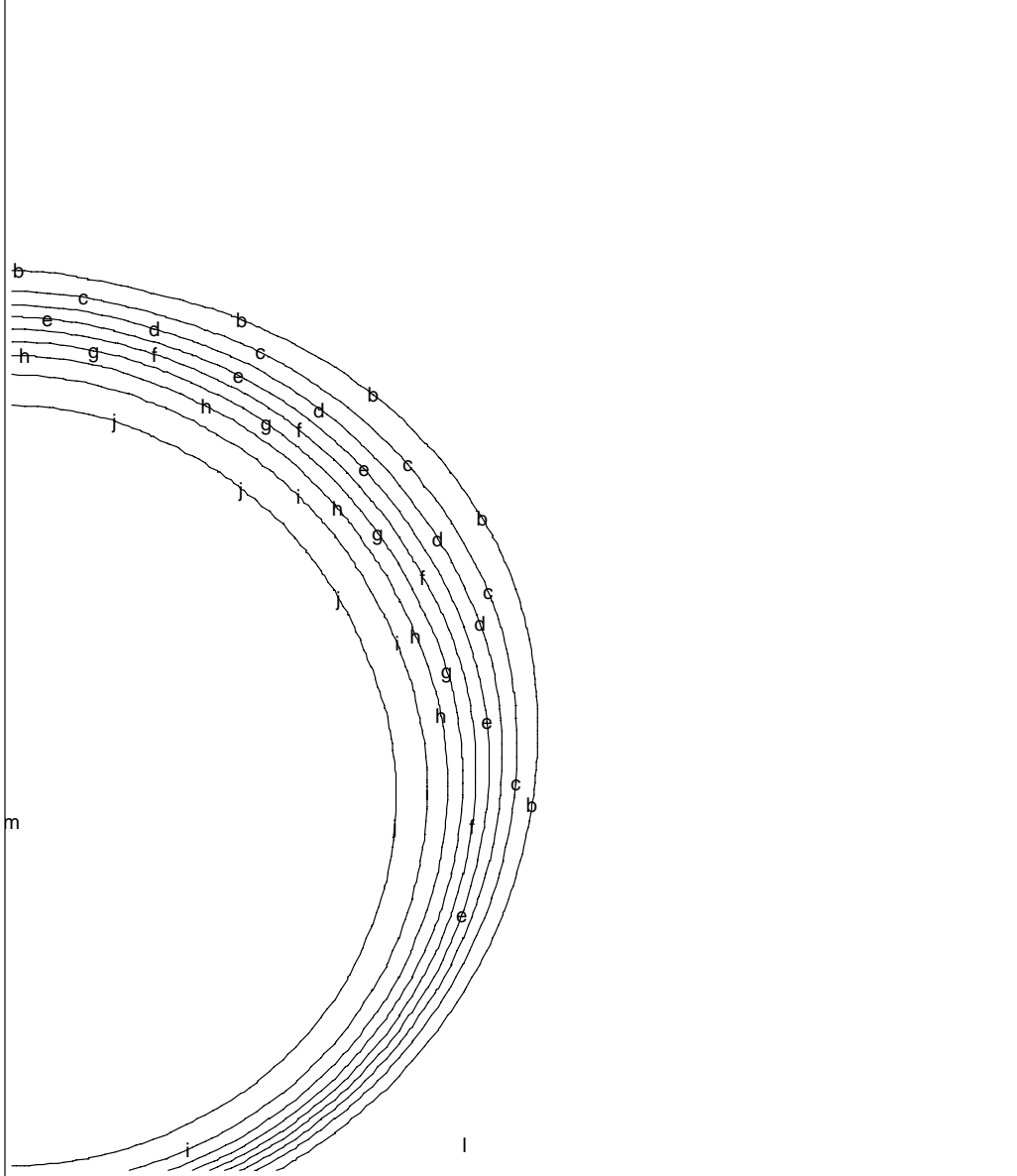


Figure 19: Mass fraction of xenon contours for the supersonic coflow case described in Section 6 at $t = 1.7105 \times 10^{-2} \mu s$.

Cell center indices 2- 80, 70- 160
vel cycle = 2500 vmax = 1.3926D+05

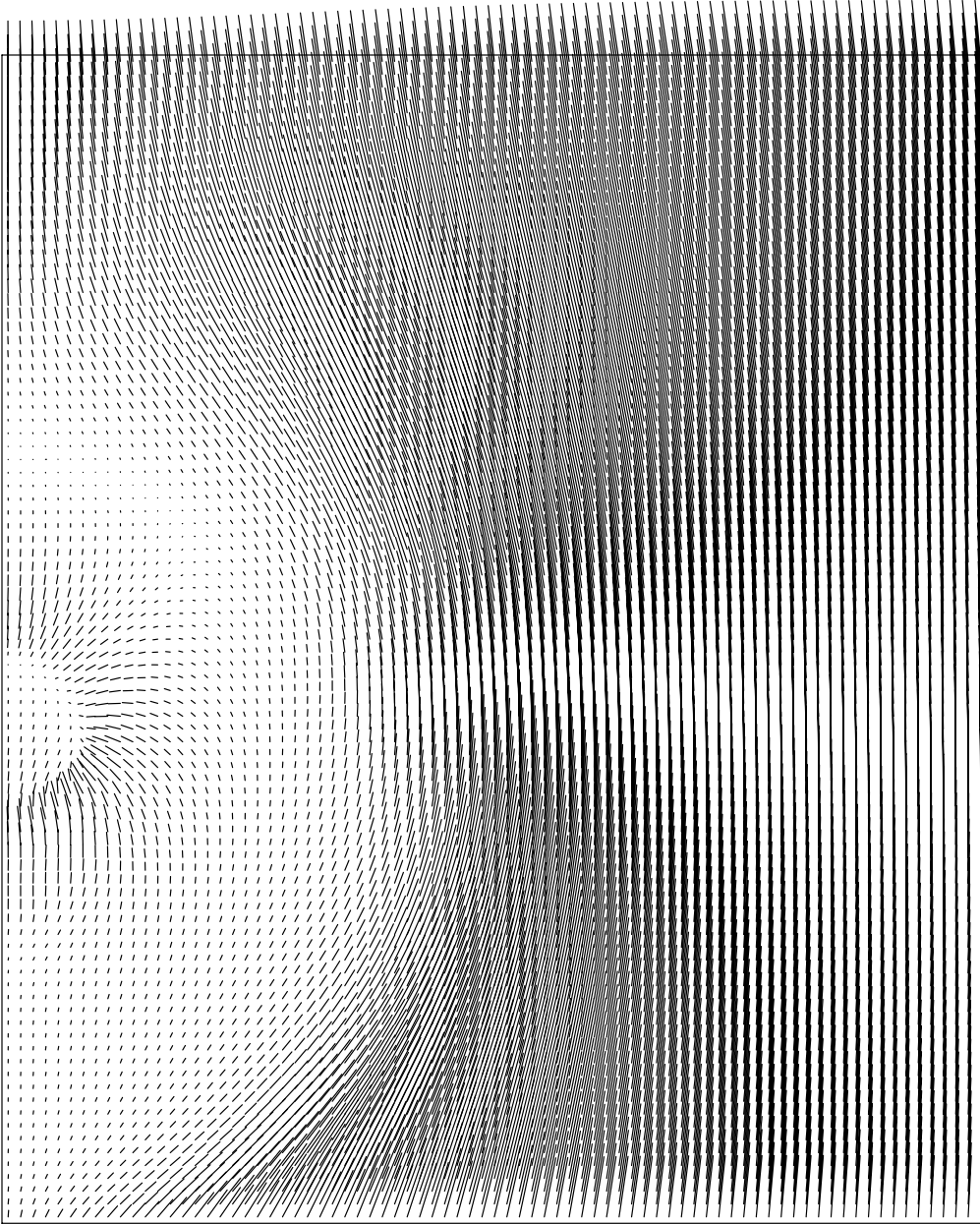


Figure 20: Velocity vectors for the supersonic coflow case described in Section 6 at $t = 2.4605 \times 10^{-2} \mu s$. The second converging shock is seen inside the nearly stagnant blob.

**Temper cycle= 2500 t= 2.460524D-08 dt= 1.000000D-11
max = 4.517645D+03 min = 2.027955D+03 dq = 2.489690D+02**

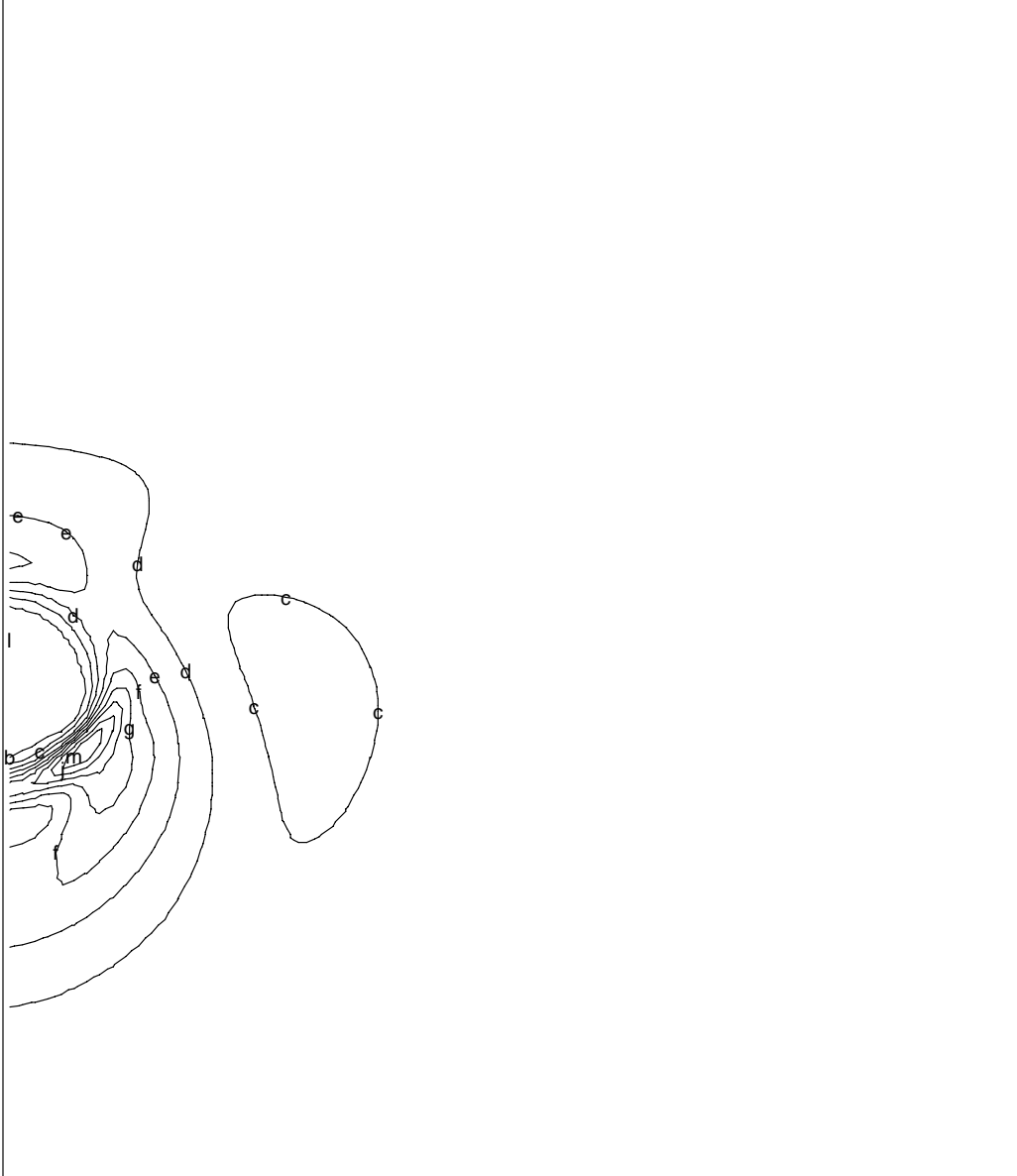


Figure 21: Temperature contours for the supersonic coflow case described in Section 6 at $t = 2.4605 \times 10^{-2} \mu s$.

Y 2 cycle= 2500 t= 2.460524D-08 dt= 1.000000D-11
max = 9.999879D-01 min = -2.344321D-07 dq = 9.999881D-02

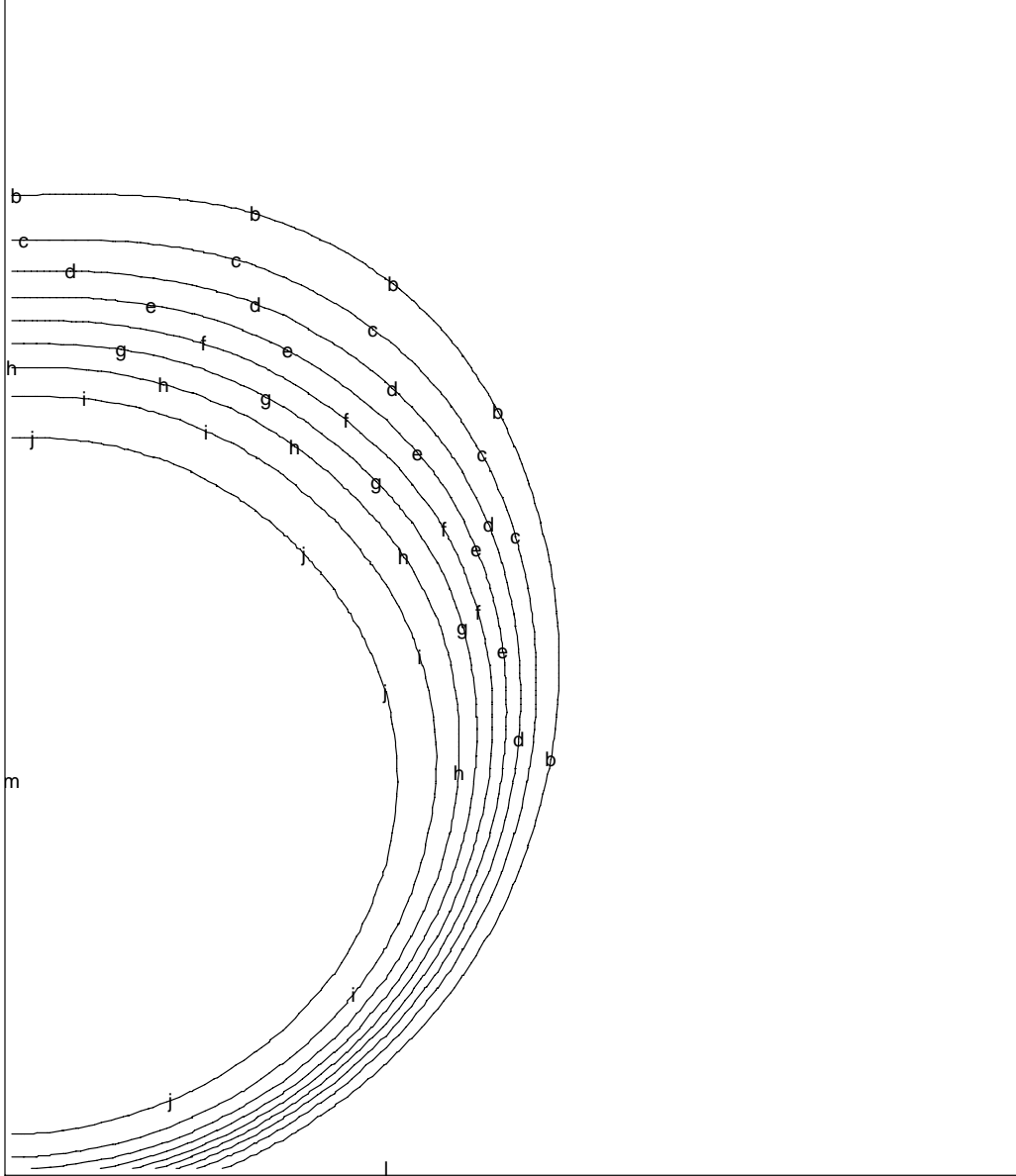
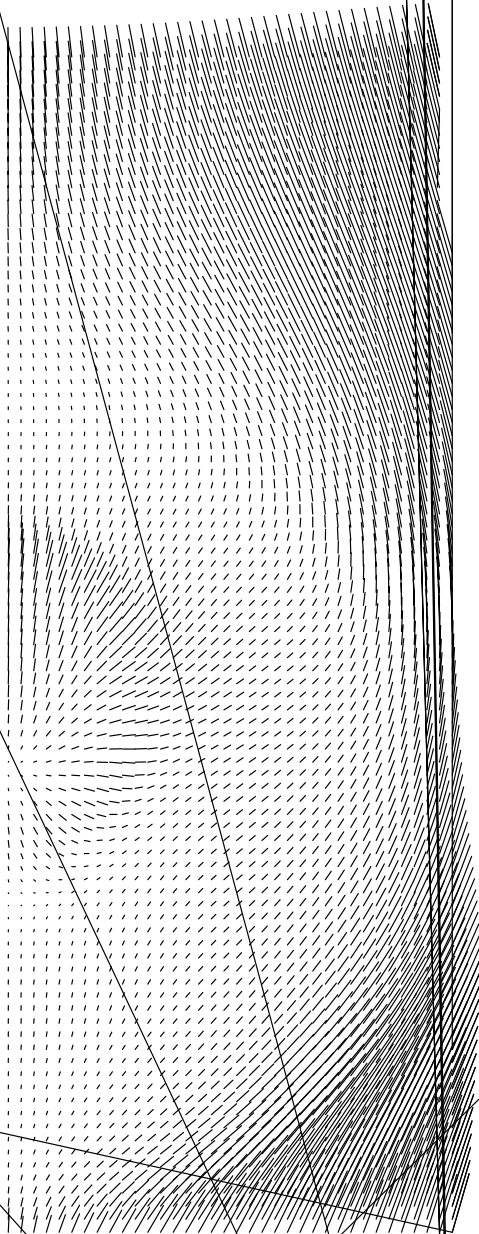


Figure 22: Mass fraction of xenon contours for the supersonic coflow case described in Section 6 at $t = 2.4605 \times 10^{-2} \mu s$.

Cell center indices 2- 80, 70- 160
vel cycle = 3250 vmax = 1.3758D+05



Pressure cycle= 3250 t= 3.210524D-08 dt= 1.000000D-11
max = 4.166915D+07 min = 1.713449D+07 dq = 2.453466D+06

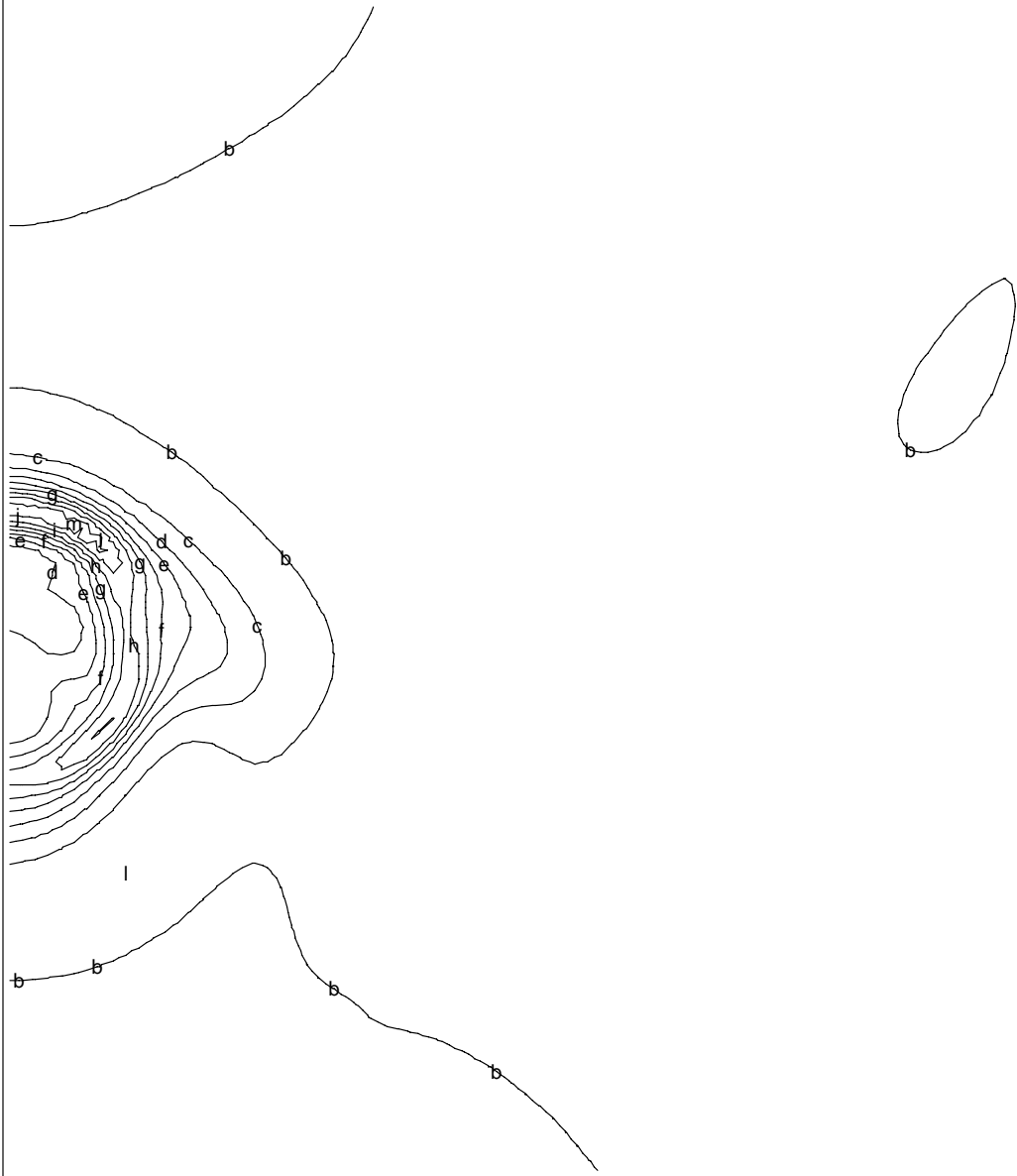


Figure 24: Pressure contours for the supersonic coflow case described in Section 6 at $t = 3.2105 \times 10^{-2} \mu s$.

Y 2 cycle= 3250 t= 3.210524D-08 dt= 1.000000D-11
max = 9.999312D-01 min = -3.308104D-06 dq = 9.999345D-02

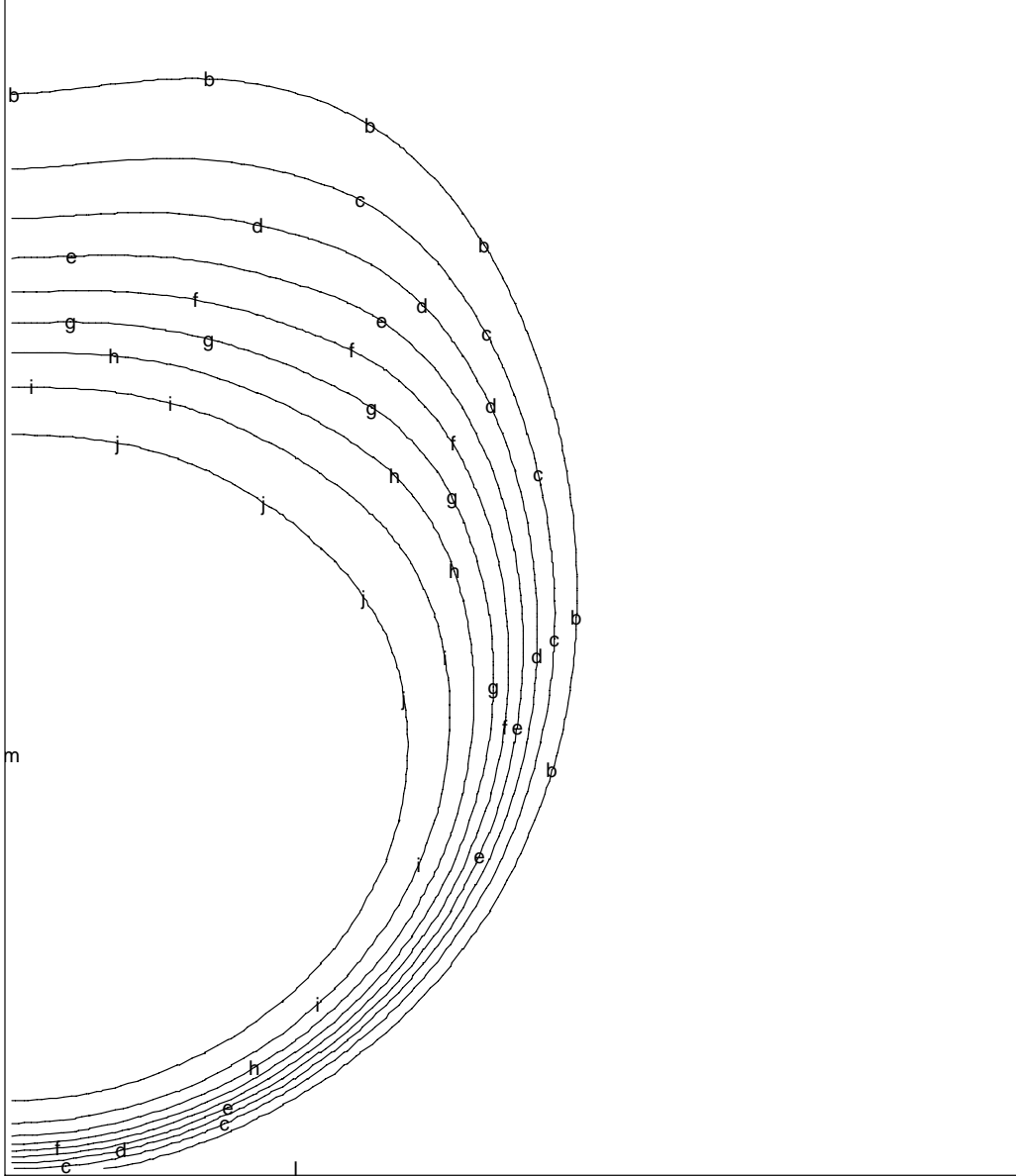


Figure 25: Mass fraction of xenon contours for the supersonic coflow case described in Section 6 at $t = 3.2105 \times 10^{-2} \mu\text{s}$.